Journal of Membrane Science 733 (2025) 124367

Contents lists available at ScienceDirect

Journal of Membrane Science

journal homepage: www.elsevier.com/locate/memsci

Semifluorinated polymer membranes by ring-opening metathesis polymerization during spin coating

Tyler D. Oddo [a], Arun Srikanth [b], Zane J. Parkerson [a], Matthew P. Vasuta [c], Co D. Quach [a], Clare McCabe [b], G. Kane Jennings [a,c,*]

[a] Department of Chemical and Biomolecular Engineering, Vanderbilt University, Nashville, TN, 37235, USA
[b] School of Engineering and Physical Sciences, Heriot-Watt University, Edinburgh, UK
[c] Interdisciplinary Materials Science Program, Vanderbilt University, Nashville, TN, 37235, USA

ARTICLE INFO

Keywords:
Pervaporation
Ethanol dehydration
Thin film composite membrane
ROMP
Fluorocarbon

ABSTRACT

Membrane technologies can offer dramatically higher energy efficiency than thermally driven separations such as distillation. The fabrication of robust, solvent-stable active layers on inexpensive supports is essential for the widespread utilization of this technology by industry. Here we show that polymer membranes incorporating a perfluoroalkyl side chain onto a hydrocarbon backbone provide remarkable enhancements in performance and stability in the dehydration of ethanol by pervaporation, even surpassing commercial perfluoropolymers. To rapidly generate these robust thin film composite membranes, we use a method termed spin coating ring-opening metathesis polymerization (scROMP) that combines the polymerization and deposition of the membrane selective layer into a 2-min process with under 1 mL of solvent per 36 cm^2 of polymer. Here, the scROMP of 5-(perfluoro-*n*-alkyl)norbornenes (NBFn) with perfluoroalkyl side chain lengths (n) of 4, 6, 8, and 10 is used to generate semifluorinated films on polyacrylonitrile (PAN) supports. pNBFn membranes exhibit greater solvent stability than their nonfluorinated polynorbornene (pNB; n = 0) counterpart while retaining excellent thermal stability, as evidenced by reduced swelling in polar and nonpolar solvents and <1 % mass loss in thermogravimetric analysis up to 130 °C. Molecular simulations show that the fluorocarbon side chains orient parallel to the surface in the bulk but more normal to the surface at the interface, consistent with experimental IR spectroscopy and wetting measurements. Of the polymers studied, pNBF8 shows the greatest performance in ethanol dehydration, obtaining a selectivity of 180 and a water permeance of 1000 GPU, while sustaining high performance for >40 h of continuous operation.

1. Introduction

Membrane-based separation of ethanol and water is of particular interest due to the rise of bio-ethanol production and its promise as a renewable fuel source [1–3]. The demand for accessible oil and gas is projected to exceed the expected growth in supply by 2040–2050 [4]. Furthermore, the use of bio-ethanol as an additive to gasoline or as an independent fuel source will help address concerns of climate change by significantly reducing CO_2 emissions from car tailpipes [5,6]. Current bio-ethanol processing involves the concentration of a 5–12 wt% ethanol solution from a fermentation broth to a stream of >99.5 wt% ethanol using a combination of distillation up to the azeotrope and pressure swing adsorption or extractive distillation for the final dewatering step [3,7]. Hybrid processes with greater energy efficiency are being developed, involving both distillation and membrane dehydration with vapor permeation or pervaporation strategies [3,8–10]. Pervaporation processes commonly use hydrophilic polymers, such as polyamide [11] or polyvinyl alcohol (PVA) [12], often with varying extents of cross-linking, to enable a water-selective separation with a chemical potential driving force [13].

Despite successes reported in the literature [1,14], the use of membrane technology is still limited primarily by two factors: tedious manufacturing processes [15] and stability [10,16,17], both of which are addressed here. Swelling reduces overall stability and performance of ethanol dehydration membranes with hydrophilic active layers [18]. A high degree of swelling can compromise the performance of the membrane by widening the polymer matrix or causing delamination of the polymer from its underlying support, both of which lead to dramatic

* Corresponding author. Department of Chemical and Biomolecular Engineering, School of Engineering, Vanderbilt University, Nashville, TN, 37235, USA.
E-mail address: kane.g.jennings@vanderbilt.edu (G.K. Jennings).

https://doi.org/10.1016/j.memsci.2025.124367
Received 9 May 2025; Received in revised form 20 June 2025; Accepted 22 June 2025
Available online 23 June 2025

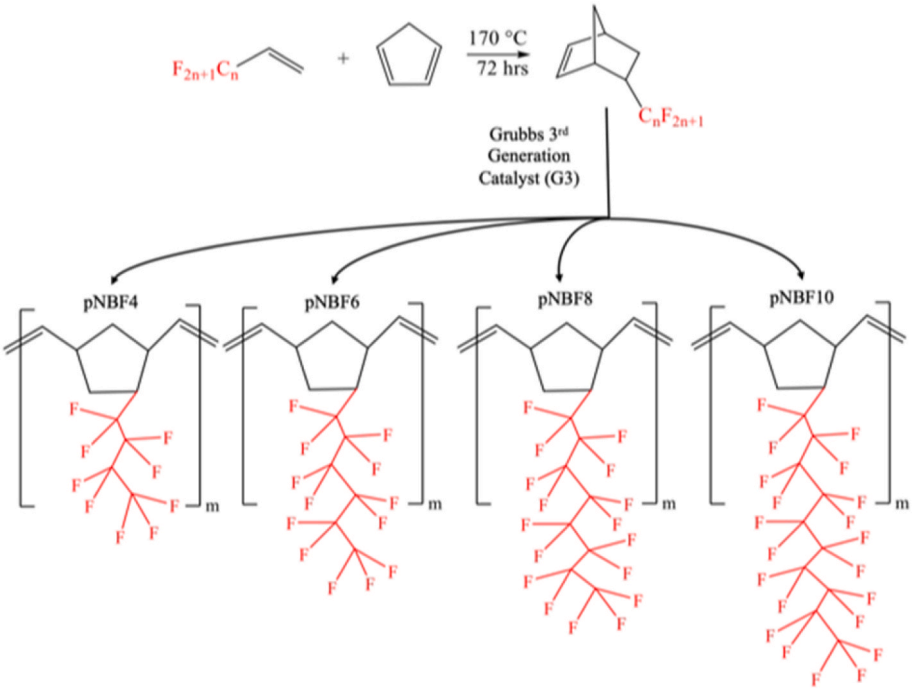

Scheme 1. NBFn monomer synthesis via a Diels-Alder reaction and ROMP of the resulting monomers with Grubbs 3rd generation catalyst.

reductions in selectivity. Alleviating the concerns of swelling typically requires the use of cross-linkers, but cross-linking can incur additional processing time and lead to chemical instabilities. For example, a common PVA cross-linking agent, glutaraldehyde, is hydrolytically labile, and cross-links can be lost at high temperatures or water concentrations [19]. Hydrophobic and inorganic membranes have been studied to ensure solvent stability without the need for cross-linking, which unlocks a facet of rapid membrane development by reducing processing steps [20,21]. More specifically, the use of amorphous perfluoropolymers has been shown to demonstrate notable polar solvent dehydration, while showcasing excellent stability [22–24]. Huang et al. [10] tested the pervaporation performance of Teflon AF 1600, Cytop, and Hyflon AD 60 for ethanol dehydration, reporting selectivities of 27, 110, and 70, respectively, while Smuleac et al. [25] reported a separation factor of 33 for an amorphous perfluoropolymer purchased from Compact Membrane Systems (CMS-3) on a polyacrylonitrile support. Amorphous perfluoropolymers have been used for other polar solvent dehydrations, such as for butanol, ethylene glycol, and even a quaternary mixture of water, ethanol, butanol, and acetone [23,24]. While these materials show promise, particularly as protective barriers for hydrophilic films [26], the use of amorphous perfluoropolymers suffers from the environmental concerns of generating excessive, harmful perfluoroalkyl substances (PFAS) due to the use of small and volatile perfluorinated monomers [27,28]. Given these concerns, we aim to take an appropriate step in limiting PFAS production by investigating the role of perfluoroalkyl side chain length on a hydrocarbon backbone to develop

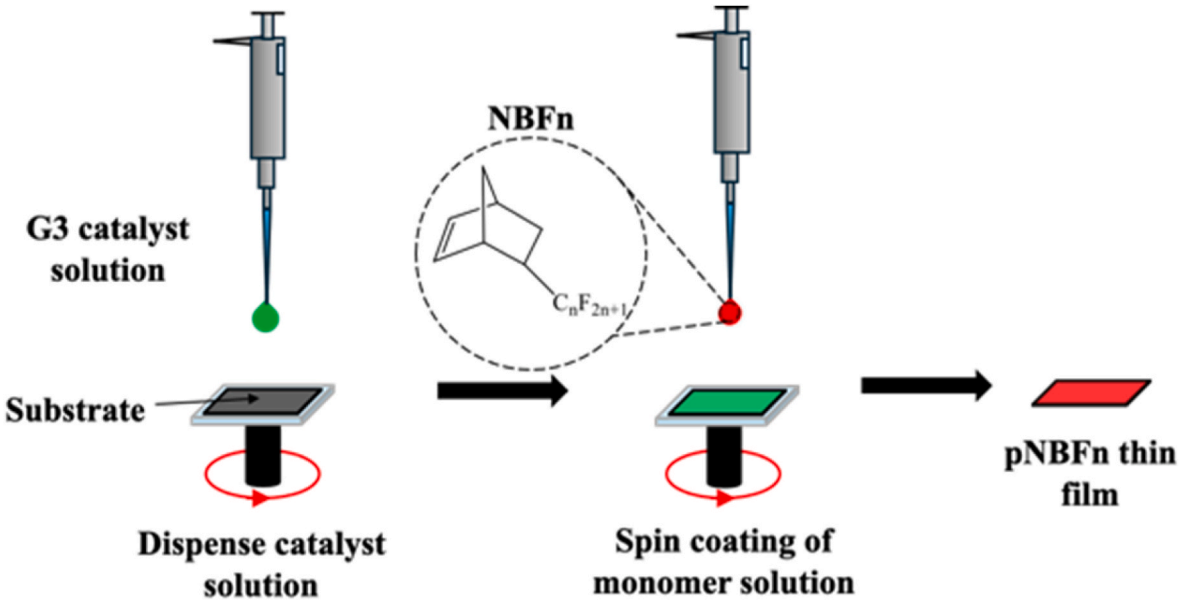

Scheme 2. Depiction of the spin coating ring-opening metathesis polymerization (scROMP) process.

semifluorinated polymer membranes for ethanol dehydration that achieve properties similar to those of amorphous perfluoropolymers.

The semifluorinated polymers utilized in this study are derived from 5-(perfluoro-*n*-alkyl)norbornenes (NBFn) to yield a hydrocarbon backbone with pendant fluorocarbon side chains (Scheme 1). Perez et al. [29] first reported the synthesis and polymerization of NBFn polymers via ring-opening metathesis polymerization (ROMP). We subsequently explored the surface-initiated ROMP (SI-ROMP) of NBFn to develop semifluorinated coatings that improve the performance of various materials [30,31]. A particular advantage of pNBFn films is that their critical surface tensions are as low as 8 mN/m, well below that of polytetrafluoroethylene (18 mN/m), an all $–CF_2-$ polymer, due to the segregation and orientation of $–CF_3$ groups at the air/film interface [32]. The SI-ROMP approach has led to the development of hydrophobic and oleophobic coatings on carbon paper [31] and gold [30] electrodes. Superhydrophobic films of these polymers were synthesized by mimicking the microstructure of *Trifolium repens* and *Aristolochia esperanzae* leaves and using a polydimethylsiloxane mold to confine the liquid monomer and catalyst [33]. More recent literature from other groups has explored the use of these materials in copolymers for their hydrophobicity, solvent stability, thermal stability, and anti-fouling capabilities. Namely, these polymers have been used as the hydrophobic constituent of block copolymers for swelling-induced pore generation [34], as a component added to graphene oxide to increase fouling resistance [35], and as a component of a polynorbornene-based copolymer for use as an anion exchange membrane [36]. In terms of membrane separation as a homopolymer, only poly (5-perfluorobutyl (norbornene)) (pNBF4) has been explored as a gas separation membrane, where the addition of the perfluoro substituent increased the permeability of gases and increased the sorption selectivity for methane-containing gas pairs [37].

In an ongoing effort to investigate the effect of fluorocarbon content on thin film and surface properties, we recently reported that random copolymers from norbornene and NBFn exhibit the surface properties of a pNBFn homopolymer with as low as 2 mol % of the partially fluorinated monomer within the norbornene and NBFn monomer mixture, yielding 7 % NBFn repeat units in the film [38]) Further, the ethanol dehydration performance of a pNBFn homopolymer can be achieved with only 50 % of the partially fluorinated monomer, yielding 63 % of NBFn repeat units in the film. Importantly, the study shows that the amount of monomeric PFAS can be greatly reduced while still achieving dense perfluroinated surfaces and effective membrane performance.

Here, we combine experiments and molecular simulations to examine the effect of perfluoroalkyl chain length on the surface properties and film structure of pNBFn homopolymer films, as well as the ethanol dehydration performance of pNBFn membranes by pervaporation. We use spin coating ring-opening metathesis polymerization (scROMP) [39] of NBFn to enable the rapid fabrication of these semifluorinated thin film composite membranes (Scheme 2). The scROMP method combines the polymerization and casting of the membrane selective layer into a rapid and low-solvent 2 min process, thereby reducing the processing time and cost and facilitating the discovery of new specialty polymeric membranes. In scROMP, a small volume of Grubbs 3rd generation catalyst (G3) in a volatile solvent is dispensed onto a spinning substrate. Then, liquid monomer (neat or in solution) is dispensed on the still spinning substrate. Polymerization occurs rapidly at the polymer/catalyst interface to generate a growing front of polymer film in the axial direction as centrifugal forces spin off unreacted monomer in the radial direction. The scROMP approach offers many advantages as a manufacturing technique, namely low polydispersity, tolerance of ambient conditions, avoidance of solvent- and time-intensive bulk polymerization associated with typical spin coating, and rapid fabrication of robust polymer films [39]. Furthermore, scROMP unlocks many opportunities for tunability, such as fabricating films with polymers that are difficult or impossible to solvate and adjusting the thickness of films between tens of microns and hundreds of nanometers by varying polymerization spin speed and monomer concentration [39]. This technique shows promise as a screening process to quickly generate polymer films with unique chemical structures, enabling the selection of the highest performing film for a desired application.

In this work, a series of 5-(perfluoro-*n*-alkyl)norbornenes were synthesized and polymerized (pNBFn) as the active layer of a thin film composite (TFC) using scROMP with perfluoro side chain lengths (n) of 4, 6, 8, and 10, along with a polynorbornene (n = 0) control (Scheme 2). Each polymer was characterized and studied to determine the effect of chain length on their film and polymer properties, solvent stability, and efficacy as a membrane. Additionally, molecular dynamics (MD) simulations were utilized to validate the theoretical and semi-empirical approaches employed and provide molecular level insight into the experimentally observed behavior. This work showcases the sensitive effect of perfluorocarbon chain length on film properties and membrane performance, as well as the ability of scROMP to screen various specialty polymers effectively and efficiently.

2. Methods

2.1. Materials

Gold shot (99.99 %) (J&J Materials) and silicon (100) wafers (University Wafers) were used to prepare gold-coated Si/SiO_2 wafers. 1H,1H,2H-perfluoro-1-hexene, 1H,1H,2H-perfluoro-1-octene, 1H,1H,2H-perfluoro-1-decene, 1H,1H,2H-perfluoro-1-dodecene, norbornene (NB), dicyclopentadiene, diethyl ether, dimethylformamide (DMF), Grubbs 2nd generation catalyst (G2), 3-bromopyridine, *trans*-3,6-endomethylene-1,2,3,6-tetrahydrophtaloyl chloride (NBDAC), and hydroquinone were purchased from Sigma Aldrich and used as received. Dichloromethane (DCM), *n*-hexane, *n*-pentane, toluene, and ethanol were purchased from ThermoFisher and used as received. Synder flat sheet polyacrylonitrile (PAN) membranes were purchased from Sterlitech, Inc. with a molecular weight cut-off (MWCO) of 30 kDa. Deionized water (16.7 MΩ-cm) was purified from a Modu-Pure system.

2.2. Synthesis of NBFn

The syntheses of 5-(perfluoro-*n*-alkyl)norbornenes with butyl, hexyl, octyl, and decyl perfluoro chains were carried out following a Diels-Alder reaction between cyclopentadiene and 1H,1H,2H-perfluoro-1-hexene (NBF4), 1H,1H,2H-perfluoro-1-octene (NBF6), 1H,1H,2H-perfluoro-1-decene (NBF8), and 1H,1H,2H-perfluoro-1-dodecene (NBF10), as described previously [29,32]. Briefly, a Parr Instruments high-pressure reaction vessel was filled with dicyclopentadiene (DCPD), hydroquinone, and the appropriate perfluoro-1-alkene in a 1.0:0.03:1.9 mol ratio. Hydroquinone was added to serve as a polymerization inhibitor [40]. The mixture was maintained at 170 °C for 72 h and the crude product purified using vacuum distillation. Percent yields ranged from ~40 % to ~60 %. The purified monomers were collected as clear/faint white liquids. The resulting endo:exo ratios were 3:1, as previously reported [32].

2.3. Synthesis of Grubbs 3rd generation catalyst (G3)

G3 was prepared as described previously [39,41,42]. Briefly, G2 and 3-bromopyridine were added in a 1:10 mol ratio to a 20 mL sealed vial. The mixture changed color from red to green after 5 min of stirring at room temperature. After the stirring process, 20 mL of pentane was added to the vial to induce the precipitation of a green solid. The filled vial was then sealed and stored in a freezer at −17 °C overnight. The precipitate was recovered via vacuum filtration and washed with pentane. The green, wet solid was dried under vacuum to recover G3 as a bright green powder.

2.4. Preparation of gold substrates

As described in previous work [42], silicon wafers were rinsed with deionized water and ethanol, then dried with nitrogen. Chromium (100 Å) and gold (1250 Å) were then evaporated in sequence onto the wafers at a rate of 2 Å/s or lower in a diffusion-pumped chamber at a base pressure of 4×10^{-6} Torr. After evaporation, the wafers were then cut to the desired size, typically 1.5 cm × 2 cm.

2.5. Processing of PAN supports

Synder Flat Sheet polyacrylonitrile (PAN) membranes with a molecular weight cutoff of 30 kDa were cut using a razor blade to the appropriate size (4 cm^2 for general characterization and 36 cm^2 for membrane testing) and stored in deionized water for at least 24 h to ensure glycerol, an additive used by the manufacturer to prevent pore collapse, was completely removed. The supports were then dried in a stream of nitrogen to remove any residual moisture.

2.6. Spin coating ring-opening metathesis polymerization (scROMP)

The polymer films generated in this study were fabricated using the scROMP method that we have recently reported [39]. In this process, a substrate, either porous (PAN) or non-porous (gold and Si/SiO_2), was placed onto a SETCAS LLC KW-4A spin coater and spun at a constant spin speed. While spinning, 200–400 μL of a 5 mM G3 solution in DCM was dispensed onto the surface and spun for 30 s at 2000 RPM, leaving behind a film of the active catalyst on the surface. Next, 200–400 μL of a monomer solution was dispensed onto the catalyst-rich substrate at 3000 RPM. The ROMP reaction was carried out for 60 s before spinning ceased, and the substrate was removed from the spin coater with a polymer film coating its surface (Scheme 2). Note that typical spin coating heuristics, such as quick deposition of the liquid onto the spinning substrate, still apply [43]. The NBFn monomers were dispensed as neat liquids, and norbornene was dispensed either as a 1 or 3 M solution in DCM. The resulting thicknesses of the films ranged from ~2 to 3 μm for films prepared from 1 M monomer concentration up to ~5–10 μm for films prepared from neat monomer. Optimizations regarding choice of spin speed for the catalyst deposition during scROMP can be found in the Supporting Information (Figs. A1 and A2).

2.7. Free-standing polymer film production

Free-standing polymer films were prepared using the scROMP process to characterize the films independently from their mechanical support, specifically for swelling and thermal studies. First, pNB and pNBFn films were produced following a typical scROMP procedure described above but on Si/SiO_2 wafers as the substrate. To induce liftoff of the pNB and pNBFn films from the wafers, the polymer-coated substrates were submerged in dimethylformamide (DMF) for 15 min. Upon removal from the liquid, the wet polymer film can simply be peeled from the surface using tweezers. The free-standing films were dried under vacuum for 30 min before being studied.

2.8. Characterization methods

To determine the chemical composition of the thin film composites generated using scROMP, attenuated total reflectance Fourier transform infrared spectroscopy (ATR-FTIR) was conducted with a Thermo Nicolet 6700 FT-IR spectrometer. This device was equipped with a liquid-nitrogen cooled mercury–cadmium–telluride (MCT) detector and a Smart iTR™ ATR attachment with a diamond crystal plate. The spectra were collected in the region of 4000–650 cm^{-1} over 256 scans at 2 cm^{-1} resolution. Spectra were analyzed using OMNIC™ software. The background scan for every sample was collected with the bare diamond crystal in air.

Contact angle goniometry was utilized to assess the wettability of the polymer films produced. A Ramé-Hart Model 100 Contact Angle Goniometer paired with a microliter syringe filled with water or hexadecane was used to measure advancing contact angles. The needle of the syringe remained inside the liquid droplet while digital photos of the static drop were taken and transferred to computers using a Diamond Multimedia VC 500 One Touch Video Capture USB, and angles were measured on both sides of the drop image using the ruler and protractor on Windows' Snipping Tool. The values reported and their error bars represent the average and standard deviation of data collected on at least three unique samples.

To determine the percent swelling of the polymers, films were either grown on gold substrates or generated as free-standing films, and then immersed in the test solution for 24 h. For films on gold, the mass of the gold-coated substrate was measured before and after the scROMP process to determine the mass of the polymer films present on the surface. Using 200 μL of 5 mM Grubbs 3rd generation catalyst in DCM and 200 μL of the neat (NBFn) or 3 M in DCM (NB) monomer with a spin speed of 1000 RPM yielded films that ranged in mass between 4 and 12 mg on 4 cm^2 gold substrates depending on the monomer being used. To generate films with greater mass, free-standing films were made using 300 μL of catalyst and monomer solutions on a 4 cm × 4 cm Si/SiO_2 substrate with spin speeds of 2000 RPM. These films weighed between 12 and 30 mg depending on the polymer being synthesized. After being removed from the test liquid, the films were briefly dabbed with a Kimwipe to remove surface droplets before the mass was measured. The values reported and their error bars represent the average and standard deviation of at least two samples.

Scanning electron microscopy (SEM) was performed using a Zeiss Merlin equipped with a Gemini II Column with an accelerating voltage of 2.00 kV. Due to the insulating nature of the samples, gold was sputtered on the surface for 20 s in an argon environment prior to imaging.

Differential scanning calorimetry (DSC) was used to determine the glass transition temperature of the polymers in this study. A TA Instruments Tzero aluminum pan was charged with ~5 mg of the polymer being analyzed and placed into a TA Instruments DSC 25. The scan routine utilized was 25–200 °C at 10 °C/min, 200 to −20 °C at −10 °C/min, and −20 to 200 °C at 10 °C/min. Cooling operations were controlled using a TA Instruments Refrigerated Cooling System 40. Before changing from heating to cooling or from cooling to heating, the final temperature of the previous cycle was held for 10 min. The first heating scan was performed to give all samples a uniform thermal history and was discarded from analysis. Results reported in this manuscript are from the second heating cycle. Data analysis was performed using TRIOS software.

The thermal stability of the polymer films was analyzed using thermogravimetric analysis (TGA). An Instrument Specialists Incorporated Simultaneous Thermal Analyzer (STA-I 650) was charged with ~10 mg of the polymer being analyzed. Care was taken to ensure the polymer samples were dried in a vacuum oven at 50 °C for 1 h before testing to ensure all solvent was removed. The samples were heated from 25 to 500 °C at 10 °C/min in an argon atmosphere. The resulting data were analyzed using Infinity Pro Thermal Analysis software.

Film thickness and topography were analyzed using stylus profilometry. A Veeco Dektak 150 stylus profilometer with a 12.5 μm radius was used to measure across 5 mm of the surface, applying 3 mg of force and utilizing hills-and-valleys detection. Thickness values reported and their errors correspond to the average and 95 % confidence interval over at least 1.5 mm of a film's surface.

2.9. Membrane pervaporation experimental setup and performance parameters

Thin film composite membranes were generated by growing pNB and pNBFn polymers onto a 36 cm^2 PAN support using scROMP. First, 400 μL of a 5 mM solution of Grubbs 3rd generation catalyst in DCM was

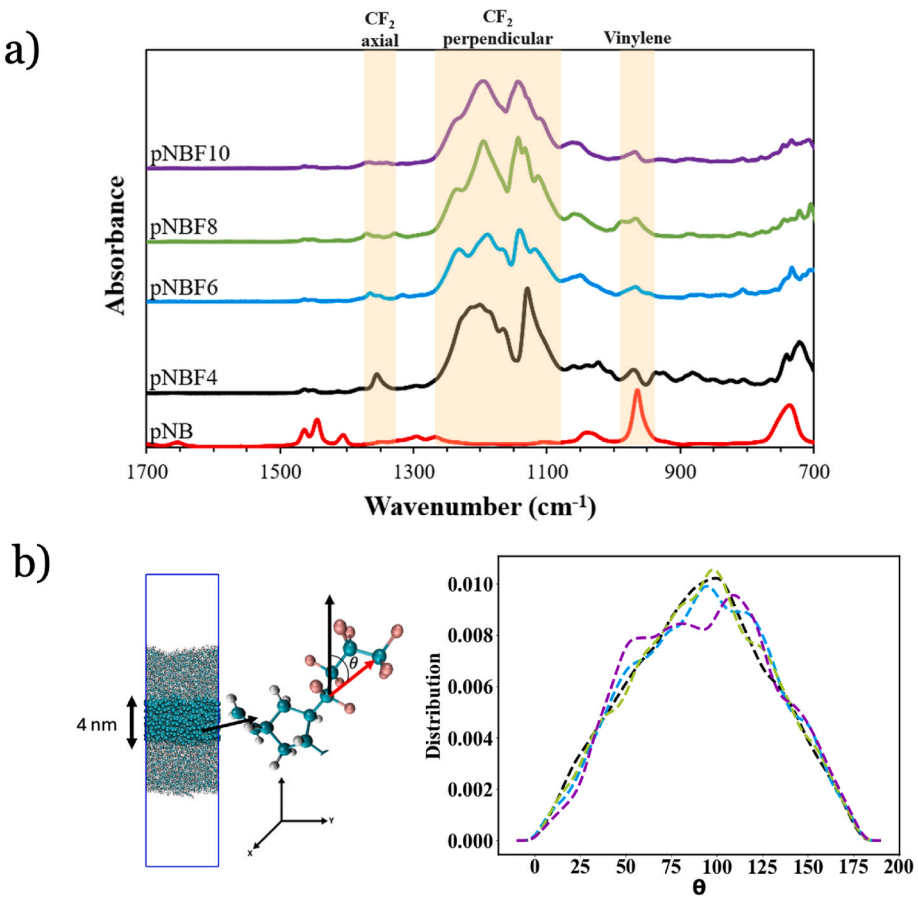

Fig. 1. (a) ATR-FTIR spectra of each polymer studied on gold substrates. Regions of the spectra due to CF_2 axial and perpendicular stretching and vinylene stretching are highlighted. The appearance of a *trans* vinylene (HC═CH) bending vibration at ~970 cm^{-1} indicates successful polymerization. (b) Simulation snapshot illustrating the central region of the simulation cell (carbon atoms are represented by cyan spheres, hydrogen atoms by white, and fluorine by purple, carbon atoms joining the two ends of the side chains are exaggerated). The angle θ (left) is determined between the normal to the x-y plane (denoted by black arrow) and the vector joining the two ends of the carbon atoms of the perfluoro chain (denoted by red arrow). The distribution of θ is shown for each polymer studied (right), with colors corresponding to those for each pNBFn film in (a). (For interpretation of the references to color in this figure legend, the reader is referred to the Web version of this article.)

dispensed onto the PAN support at a spin speed of 2000 RPM followed by 400 μL of the neat (NBF4 = 4.6 M, NBF6 = 3.9 M, NBF8 = 2.7 M, and NBF10 = 2.6 M) or 1 M (NB in DCM) monomer. All solutions were made with DCM as a solvent to allow fast evaporation and effective dissolution. The spin speeds were chosen based on a uniformity study described in Supporting Information (Figs. A1 and A2). The manufactured membranes were tested using the setup depicted in Scheme D1. A 1 L glass feed tank was filled with 250 mL of 90 wt% ethanol and heated to the desired operating temperature using an oil bath. The temperature of the feed was maintained throughout the experiment. FreelinWade nylon tubing was used to connect the feed to an Iwaki MD-10L magnet pump and ultimately to a Sterlitech CF016 cross flow membrane cell, which exposed 16 cm^2 of the membrane. The vacuum pressure on the permeate side of the membrane averaged ~3 kPa and was controlled using a screw valve and an Edwards E2M5 vacuum pump. The permeate was collected using a cold trap in liquid nitrogen. Experiments were typically run for 6 h to ensure sufficient permeate volume was collected. After shutting down the vacuum pump, the permeate was allowed to warm up in a closed system to room temperature to prevent humidity in the air from condensing inside the cold trap. The temperature and vacuum pressure of the setup were constantly monitored using a laboratory thermometer and a pressure gauge. The retentate was cycled back into the feed tank.

Parameters used to gauge the performance of the membranes include flux (J), water permeance ($\frac{P^G_{H_2O}}{l}$), selectivity (α), separation factor (β), and permeate ethanol concentration. Flux was calculated by measuring the mass of permeate collected using a balance and dividing it by the operation time of the membrane and the surface area of the testing cell (16 cm^2). The mass fraction of ethanol in the permeate was calculated using an Atago PAL-34S pocket refractometer. For concentrations outside of the measurement range of the instrument, an aliquot of the permeate was diluted with a known amount of water, and the concentration was back calculated. α, β, and $\frac{P^G_{H_2O}}{l}$ are measures of the separation efficiency of the membrane and are respectively defined as [44]

$$\alpha_{ik} = \frac{J_i/(p_{io} - p_{il})}{J_k/(p_{ko} - p_{kl})} = \frac{J_i/\left(x_i\gamma_i p_i^{sat} - p_{il}\right)}{J_k/\left(x_k\gamma_k p_k^{sat} - p_{kl}\right)} \quad (1)$$

$$\beta_{ik} = \frac{y_i/y_k}{x_i/x_k} \quad (2)$$

$$\frac{P^G_{H_2O}}{l} = \frac{J_{H_2O}}{\left(p_{H_2O,o} - p_{H_2O,l}\right)} \quad (3)$$

where J is the molar flux, x is the mole fraction on the feed side, p is the partial pressure, γ is the activity coefficient of a species in the feed solution, y is the mole fraction on the permeate side of the membrane, l represents the membrane thickness, and $P^G_{H_2O}$ is the permeability of water. Species i represents water and species k represents ethanol. Subscripts of o and l represent the feed and permeate sides of the membrane, respectively. Both α and β are reported here because β is

more commonly reported in the membrane literature, but α more accurately decouples variations in membrane performance due to vapor-liquid equilibrium effects from the fundamental permeation properties of the film [44].

2.10. Molecular dynamics simulations

The mbuild python package [45,46] included in the MoSDeF tool suite [47] was used to construct pNB and pNBFn chains with n = 4, 6, 8, and 10 and prepare the initial system configurations. The polymer chains were end-capped using vinyl groups. Each chain consisted of 30 repeat units with molecular weight ranging between 2.8 and 18.4 kDa, with 2.8 kDa corresponding to pNB and 18.5 kDa to pNBF10. The bulk polymer systems for pNB, pNBF4, pNBF6, pNBF8 and pNBF10 consisted of 60, 32, 27, 23 and 21 chains, respectively. The all-atom optimized potential for liquid simulations (OPLS-AA) [48] force field was used to describe the inter (non-bonded) and intramolecular interactions and implemented using Foyer [49] within the MoSDeF toolsuite. Three independent replicas were simulated for each polymer system studied to reduce the statistical uncertainties in the simulated properties. All simulations were performed using GROMACS [50] version 2023.2.

The bulk polymer systems were first equilibrated in the NVT ensemble at low temperature (15 K) for 1 ns to prevent the polymer chains from collapsing. Next, the 21-step equilibration protocol established by Lauren et al. [51] in which a bulk polymer system is transformed from an initial gaseous phase to a condensed phase was followed. Briefly, the polymer system undergoes gradual compression and expansion, as well as sequential heating and cooling cycles, to achieve a condensed phase density corresponding to the desired temperature of 300 K and pressure of 1 atm.

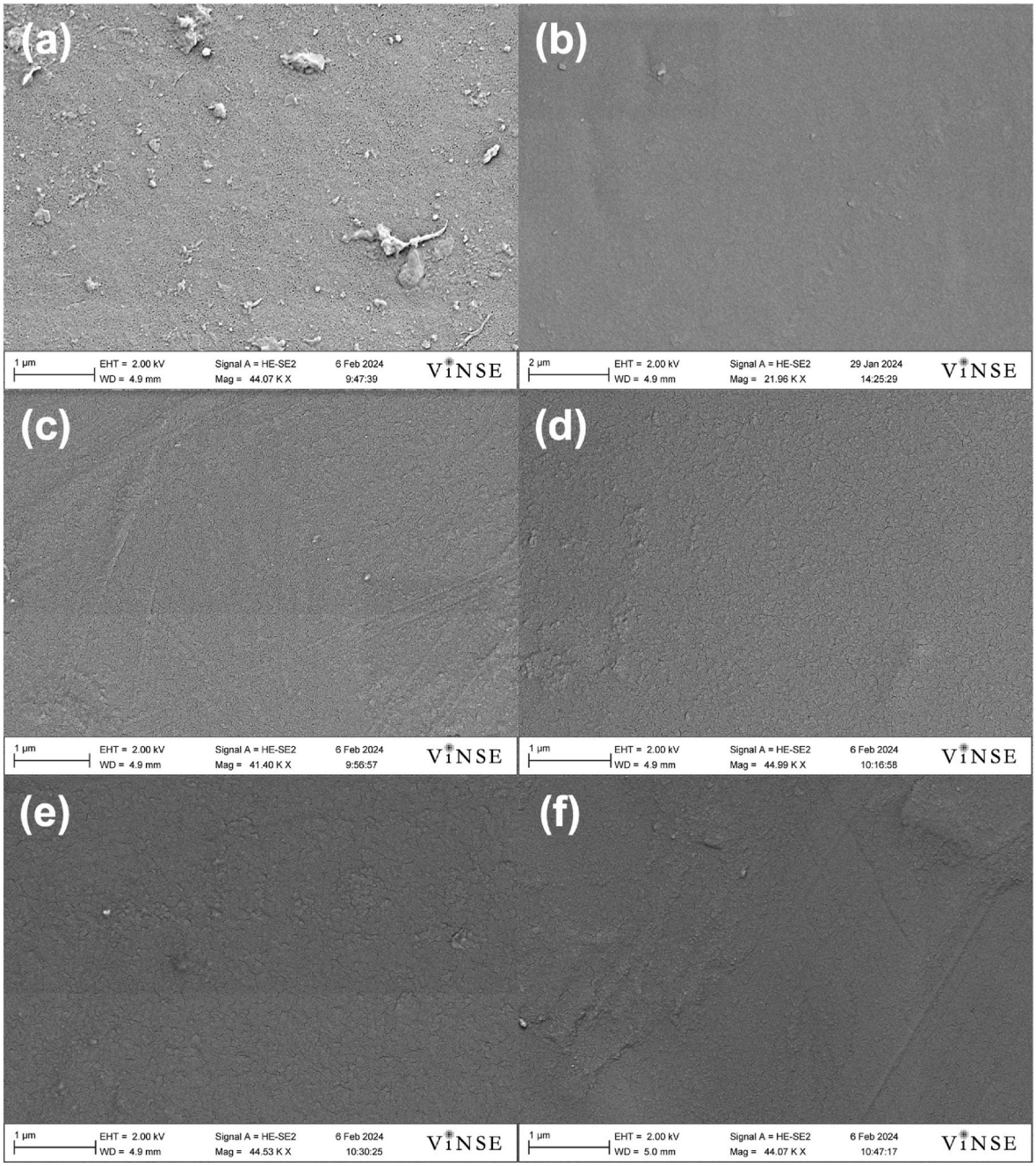

Fig. 2. SEM images of (a) bare PAN and films of (b) pNB, (c) pNBF4, (d) pNBF6, (e) pNBF8, and (f) pNBF10 on 30 kDa MWCO PAN.

Thin films of pNB and pNBFn were constructed following Zifeng et al. [52]. The equilibrated bulk polymer systems were then replicated twice in the z-dimension to obtain continuous films of ~14–16 nm (see Table H2 in the SI). Structureless Lennard Jones walls ($\sigma = 0.355$ nm, $\varepsilon = 0.318$ kJ/mol) were placed on both sides of the z-dimension, and the system was subjected to the same 21-step equilibration protocol [51] as for the bulk polymer systems. Subsequently, the walls were removed and vacuum added above and below the film to create a free-standing film. Full details of the equilibration processes for both the bulk systems and thin films studied are provided in the SI.

Properties of bulk polymer models, such as density and free volume, were determined alongside structural properties, such as the radial distribution function and the torsional and angle distributions of the constituents on the polymer backbone. For the thin film simulations, the surface composition and orientation of side chains were determined. Additional details of the methods used for property calculations are provided in the SI. The GROMACS files and python codes necessary to reproduce the simulation results can be downloaded from https://github.com/PTC-CMC/PNBFN_signac.

3. Results and discussion

3.1. Chemical composition and successful polymerization

ATR-FTIR spectroscopy was conducted on pNB and pNBFn films to analyze film composition and confirm a successful polymerization by scROMP. Fig. 1a displays the resulting spectrum of each polymer from 1700 to 700 cm^{-1}. Each film with a perfluoro side chain exhibits strong perpendicular CF_2 stretching from ~1300 to 1100 cm^{-1} and faint axial CF_2 stretching around 1350 cm^{-1}, with a slight increase in wavenumber as the fluorocarbon chain grows in length. These results match previous experiments [32] and suggest that the fluorocarbon chains orient mostly parallel with respect to the surface in the bulk of the film. This directionality can be expected because the large perfluoro chains make up 70 % (pNBF4) to 85 % (pNBF10) of the total mass and ~51 %–~72 % of the total volume of the macromolecule. Simulations further support this chain structure as shown in Fig. 1b, which shows the distribution of the angle θ between the vector joining the two ends of the carbon atoms of the perfluoro chains located in the central region and the normal to the x-y plane. While the distribution of θ broadens as the length of the fluorinated side chain increases from F4 to F10, indicating that packing is disrupted as chain length increases, for all systems the mean is centered around 90° with a standard deviation of 38°, indicating that the perfluoro chains are predominantly parallel to the surface in the bulk of the film.

Fig. 1a also shows the presence of a vinylene (HC═CH) stretching peak near ~970 cm^{-1} that is characteristic of the *trans* orientation of the HC═CH bond [53]. Although this peak is muted for pNBFn polymers compared to the strong CF_2 stretches, the same peak is observed for these materials. Thus, the 970 cm^{-1} peak serves as an indicator that the norbornene ring structure has been opened, thereby signaling a successful polymerization.

3.2. scROMP thin film composite topography and cross section

Fig. 2 shows SEM top-view images for a bare 30 kDa MWCO PAN support before and after coating with pNB and pNBFn with n = 4, 6, 8 and 10. These images confirm that the scROMP process produces a dense, continuous film across the PAN support that blocks the pores of the PAN. Further examination of the topography of polymer films made with neat monomers on PAN was conducted using stylus profilometry and compared to that of a pristine support. The polymer films measured ~1–10 μm thick and matched the rough topography of the PAN support. A representative profile of a pNBF6 film exhibiting a thickness of 8.2 ± 1.1 μm is shown in Fig. 3a with a scan of the bare PAN support topography accompanying it. A comparison of these two scans suggests that the film grown by scROMP adopts the rough topography of the underlying PAN. To further illustrate that the scROMP films adopt the topography of their underlying supports, a scan of pNBF6 on gold is displayed in Fig. 3b. This scan depicts a much smoother film with an average roughness of only ~150 nm compared to ~1100 nm for the film generated on PAN. Additionally, the thickness of the film on gold ranged between 7.7 ± 0.2 μm rather than the broader values of 8.2 ± 1.1 μm for the polymer layer on PAN.

In addition to information regarding the topography of pNBFn films made using scROMP, cross-sectional SEM and EDS images (Fig. 4) show the distinct layers of the thin film composite. In Fig. 4a, a dense polymer layer composed of pNBF8 is atop PAN, which is supported on a nonwoven polyester backing (not shown). The microscale separation between the layers is attributed to frictional stress caused by fracturing the sample with a razor blade at room temperature; attempts at cryo fracture were unsuccessful in cleaving the polyester backing. Despite the slight separation between the layers shown here, we have observed that polymer films formed by scROMP are difficult/impossible to remove from PAN, whereas many films by scROMP can be removed more readily from an unmodified, nonporous substrate [39]. To further examine the distribution of pNBF8 throughout the thin film composite, energy dispersive x-ray spectroscopy (EDS) was used to detect carbon, fluorine, and nitrogen in Fig. 4b, c, and 4d, respectively. Fig. 4b shows that carbon is expectedly present throughout, Fig. 4c shows that fluorine is present

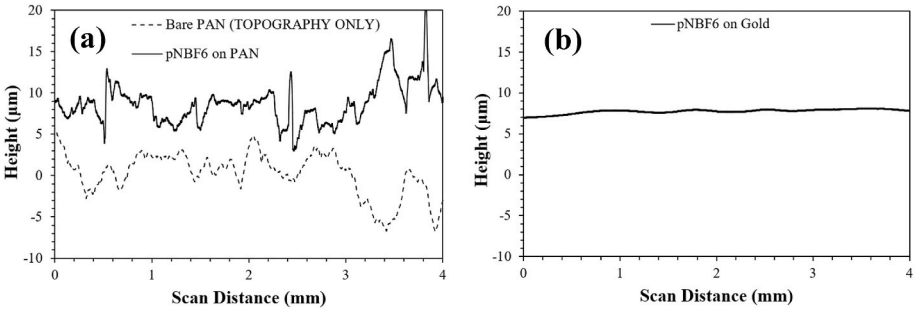

Fig. 3. Profilometric scans of a pNBF6 polymer film fabricated on (a) PAN and on (b) gold, showing that the topography of the polymer film conforms to that of the surface it was generated on.

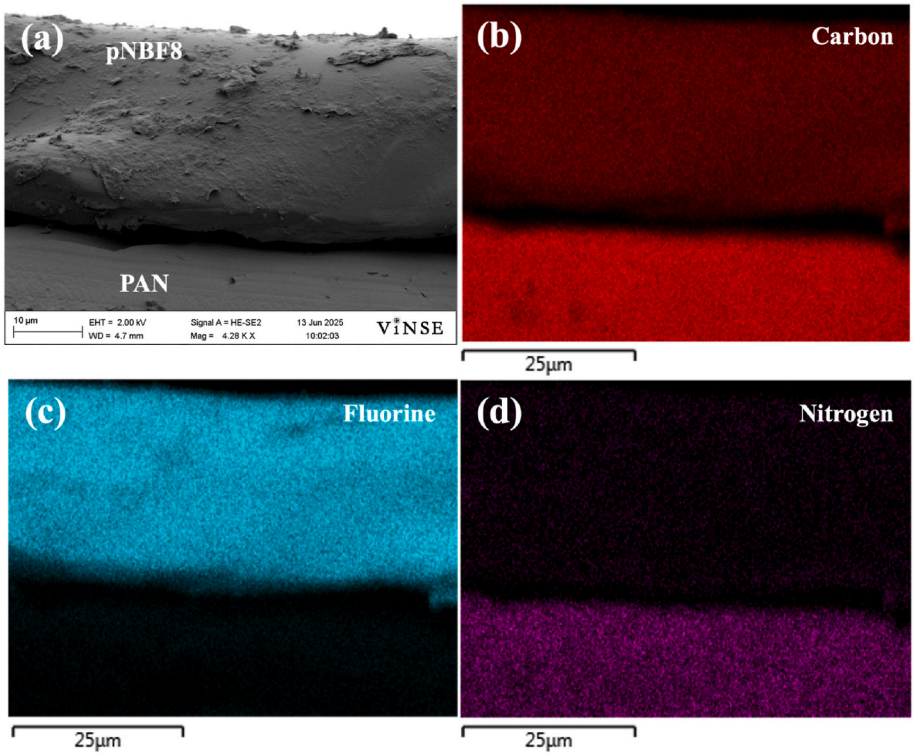

Fig. 4. (a) Cross sectional SEM image of pNBF8 and EDS of (b) carbon (red), (c) fluorine (cyan), and (d) nitrogen (purple) on 30 kDa MWCO PAN. The NBF8 monomer was deposited at 2000 rpm. The electron image map of the EDS is shown in Figure E2, Supporting Information. (For interpretation of the references to color in this figure legend, the reader is referred to the Web version of this article.)

solely in the pNBF8 top film and not in the PAN layer, and Fig. 4d shows that nitrogen is expectedly present in the PAN layer. The greater film thickness (~25 μm) here versus that in Fig. 3a (~10 μm) is due to the use of a slower monomer spin speed (2000 vs 3000 rpm). A lower magnification SEM image of a pNBF8 film prepared at a monomer spin speed of 3000 rpm (see Figure E1, Supporting Information) shows a much thinner film (<15 μm) with no separation of the pNBF8 from the PAN.

3.3. Bulk density and thermal properties

Table 1 reports the density of the bulk polymer systems simulated at 300 K in comparison to the available experimental data for the monomers and polymers [37,54]. The simulations show that density increases as the side chain length increases and is consistent with the experimental results of monomer density and the limited reports of polymer density. This increase in density with chain length is consistent with the much higher density of perfluorocarbon chains than that of the unmodified polynorbornene repeat structure and their increased mass fraction in the film as chain length increases. The agreement obtained suggests that the forcefields used adequately model the experimental polymer samples (see also Section I in the supporting information) and are suitable for use in further characterization and analysis studies.

Table 1
Experimental density for NBFn monomers and both simulated and experimental density for pNBFn polymers at 300K.

	Monomer Density (experimental)[a] (kg/m^3)	Polymer Density (simulated) (kg/m^3)	Polymer Density (experimental)[b] (kg/m^3)
pNB	955[a]	954 ± 1	999 [37,54]
pNBF4	1355 ± 34	1489 ± 4	1530 [37]
pNBF6	1526 ± 38	1574 ± 2	–
pNBF8	1622 ± 41	1638 ± 1	–
pNBF10	–	1687 ± 5	–

[a] Error values here represent the error of the method as calculated by gravimetrically obtaining the density of a solvent (hexane) with a known density.
[b] Reported value from literature with no error range.

The thermal properties of the polymers were measured experimentally using DSC and TGA. TGA was conducted to examine how the perfluorocarbon moiety contributed to the burn-off of the polymer films at high temperatures (Fig. 5). The TGA results reveal that the temperature at which rapid burn-off begins (T_{onset}) and the temperature at which the maximum burn-off rate is achieved (T_{max}) are indistinguishable for each polymer in the pNBFn system, while pNB exhibited a slightly higher thermal stability. This difference in thermal behavior indicates that the decomposition pathway for the partially fluorinated polymers occurs via a related mechanism, possibly involving the HC—CF_2 bond. Despite a lower temperature of decomposition than for pNB, the results show that throughout the range of typical operating temperatures for ethanol dehydration membranes (no higher than 130 °C according to Huang et al. [10]), the polymers are all highly stable. This thermal stability ensures that the membranes will remain robust and operational under typical temperatures for ethanol dehydration via pervaporation and prevent molecular PFAS generation that would accompany thermal decomposition.

DSC was utilized to determine the glass transition temperature (T_g) of each polymer. For membranes, the glass transition temperature is important because polymers that are glassy at the operating temperature contain non-equilibrium free volume, which can contribute to a more diffusion-controlled separation biased towards smaller molecules [55]. The DSC of pNB served as a control since it is a well-studied polymer with an expected glass transition temperature between 35 and 45 °C [56,57]. As shown in Table 2, pNB grown using the scROMP process has a T_g of 44 °C, which falls within the expected range. The addition of a short fluorocarbon chain increases T_g to 64 °C for pNBF4, in agreement with literature [37], but increasing the fluorocarbon length further decreases T_g to ~45 °C for chain lengths of 6, 8, and 10 carbons. This trend of T_g with fluorocarbon chain length is related to the stiffness of the

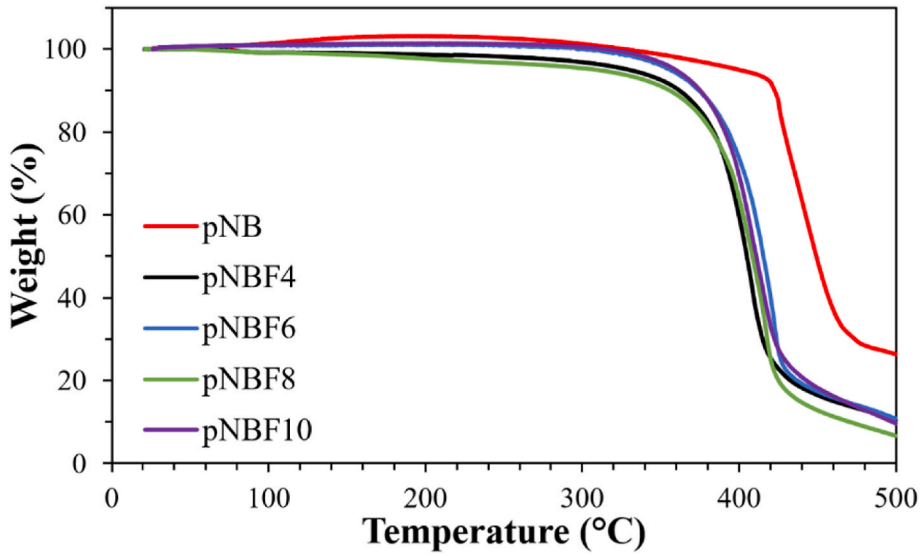

Fig. 5. TGA curves of the pNB and pNBFn polymers studied. Measurements were taken in an argon atmosphere with a heating rate of 10 °C/min.

Table 2
Summary of the thermal properties of the polymers studied, including the temperature at which rapid burn-off begins (T_{onset}) and temperature at which the maximum rate of burn-off is achieved (T_{max}) in TGA and the glass transition temperature (T_g) in DSC, all based on one sample for each polymer studied.

Polymer	T_{onset} (°C)	T_{max} (°C)	T_g (°C)
pNB	418	442	44
pNBF4	382	409	64
pNBF6	378	408	48
pNBF8	380	410	44
pNBF10	383	411	47

fluorocarbon side chains and is different from that of more flexible hydrocarbon side chains, in which T_g is consistently and dramatically reduced with longer side chains due to internal plasticization [58].

Based on these thermal experiments, pNBF4 will be in a glassy state for many typical ethanol dehydration operating temperatures, while the remaining polymers in the system will likely be rubbery. This difference could lead to different separation mechanisms and performances for pNBF4 as compared to its counterparts.

3.4. Local structural analysis and free volume properties

Increasing side chain length can significantly alter local structural properties and free volume, which in turn can influence the transport of small molecules. The size and stiffness of the side chain can be quantified by the characteristic ratio, C_{NSC}, given by [59]

$$C_{NSC} = \frac{< R_{NC}^2 >}{nl^2} \quad (4)$$

where n is the number of bonds in the side chains, l is the length of the bond joining two successive carbon atoms in the side chain (1.57 Å), and $< R_{NC}^2 >$ is the ensemble averaged end-end squared distance.

In Fig. 6a, C_{NSC} is plotted as a function of side chain length for the pNBFn systems studied and shows that the relative size and stiffness increase with chain length. This trend, in-part, likely contributes to the T_g insensitivity when the chain length is increased above 4, in contrast to the sharp decrease in T_g with increased chain length for all-hydrocarbon systems.

The increase in side chain size implies an increase in steric hindrance that can prevent backbone chains from approaching each other, often termed the “shielding effect” [60]. To further investigate this behavior, the interchain radial distribution functions of backbone carbon atoms in the cyclopentylene rings, $g(r)_{bb}$, of the pNBFn polymers were computed and are shown in Fig. 6b. The size of the exclusion zone (i.e., where $g(r)_{bb}$ is zero) is found to not be significantly influenced by chain length, suggesting the near absence of this effect in the pNBFn polymers studied. A systematic decrease in the first peak with increasing chain length is observed, suggesting backbone-backbone interactions become weaker as the chain length is extended.

Interactions between side chains is another important structural feature that can influence the transport of small molecules. To analyze side chain interactions, the interchain radial distributions of the carbon atoms in the side chains, $g(r)_{SC-SC}$ are computed and shown in Fig. 6c. At shorter distances (~0.6 nm), $g(r)_{SC-SC}$ decreases when moving from pNBF4 to pNBF10 indicating that side chain interaction is lower in pNBF10 compared to that of pNBF4. Fig. 6b and c further show the absence of long range order, confirming that the simulated polymer systems are amorphous.

The free volume distribution (also known as pore size distribution, PSD) and other free volume properties such as FAV (fractional available free volume i.e., free volume available for a probe of radius 1.4 Å, since this roughly corresponds to the size of a water molecule), PLD (pore limiting diameter), LCD (largest cavity diameter), and FFV (fractional free volume available for a probe of zero radius) of the bulk pNBFn polymer models were calculated at 300 K. The PSDs of the polymers studied are reported in Fig. 6d with other free volume properties reported in Table 3. Fig. 6d shows that the PSDs of the polymers are unimodal with pore sizes ranging from 1.8 to 6 Å , suggesting that these polymers are microporous. The width of the PSD is narrower for pNB as compared to the fluorinated polymers, indicating that pore sizes are somewhat more uniform for pNB.

From Table 3, we note that the calculated FFVs of the pNBFn polymers range from 35 to 38 % and are in good agreement with values reported for other glassy polymers [61]. Additionally, all the free volume properties reported increase with the addition of perfluoroalkyl side chains, with a weak dependence on side-chain lengths beyond 4. The FFVs reported are significantly higher than the values predicted by the Bondi semi-empirical approach, which has been observed previously for other polymers [62] and is attributed to the fact that the universal packing coefficient used in the calculation of the FFV^{Bondi} values does not reflect the true molecular packing. We also note from Table 3 that the PLD, which is the largest probe particle size for which there is a percolating pore across the system, is smaller than the size of a water molecule for all polymers studied at 300 K [63]. This indicates that any

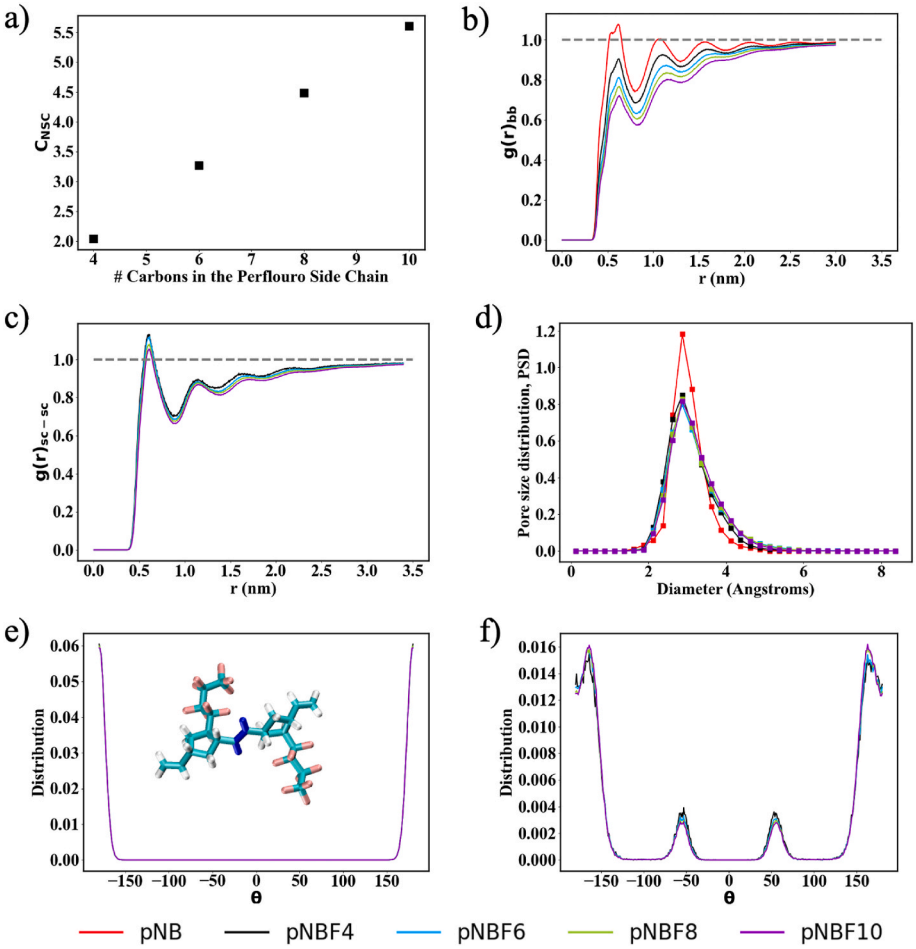

Fig. 6. (a) Characteristic ratio of the side chains, C_{NSC} (uncertainties are smaller than the symbols), (b) interchain radial distribution of the carbon atoms in the cyclopentylene rings, (c) interchain radial distribution of the carbon atoms in the side chains (each curve represents an average of three replicas), (d) pore size distribution of pNBFn polymers (each curve represents an average of 9 configurations drawn from three replicas over a period of 100 ns, see SI for details), (e) probability distribution of the torsion angles formed by the carbon atoms (denoted in blue, see inset) along the backbone, (f) probability distribution of the torsion angles formed by the carbon atoms along the sidechains. (For interpretation of the references to color in this figure legend, the reader is referred to the Web version of this article.)

transport of solvent must be facilated by swelling induced enlargement of the pores. The higher value of LCD for pNBFn compared to pNB indicates that pNBFn membranes can accommodate molecules of larger size.

Fig. 6e shows the distribution of the torsions involving the carbon atoms joining two adjacent monomers on the backbone (see inset of Fig. 6e). The chain length of the side chains is found to have no significant influence on the backbone flexibility. *Cis* conformations induce kinks in the backbone that can disrupt molecular packing and can therefore increase the free volume. Fig. 6e shows no evidence of this occurrence as the torsion angles are in the all-*trans* conformation (i.e., $\theta = 180^{o}$). The torsional strain associated with conformational flexibility of the cyclopentylene rings is another factor that can affect molecular packing. We find that side chain susbitituion has no influence on the conformational flexibility of the backbone cyclopentylene rings of the pNBFn polymers (see **Section J, Supporting Information**).

The distribution of the torsion angle formed by the carbon atoms in the side chains is shown in Fig. 6f and demonstrates that the side chains preferentially adopt *trans* over guache conformations (± 60°). Furthermore, the gauche conformations are found to decrease as chain length increases. This could lead to increased packing efficiency as chain length increases, since free volume tends to decrease with decreases in "gauch defects," and hence play a role in the observed insensitivity in the FAV with chain length.

Table 3
Free volume properties calculated from MD simulations at 300 K for the pNB and pNBFn systems studied and the Bondi group contribution-based approach (FFV^{Bondi}). The simulated properties reported are fractional free volume (FFV) accessible to a point probe (i.e., probe size of zero radius), the fractional free volume accessible to a water probe (FAV), the pore limiting diameter (PLD), and the largest cavity diameter (LCD). Uncertainties in FAV and FFV calculated from MD simulations are not reported as they are negligible.

Polymer	FFV	FAV	FFV^{Bondi}	PLD (Å)	LCD (Å)
pNB	0.35	0.028	0.111	1.31 ± 0.04	4.7 ± 0.3
pNBF4	0.38	0.079	0.173	1.62 ± 0.01	5.6± 0.1
pNBF6	0.38	0.084	0.183	1.61 ± 0.02	6.0 ± 0.1
pNBF8	0.38	0.087	0.189	1.70 ± 0.06	5.6 ± 0.1
pNBF10	0.38	0.088	0.193	1.66 ± 0.01	6.0 ± 0.2

3.5. *Surface composition, surface chain conformation, and surface wettability*

Surface properties such as compositions and chain conformations within the depth of a few nanometers from the air-polymer interface can be noticeably different when compared to the bulk phase (Fig. 7a). These unique surface properties can influence the adsorption characteristics and wettability of thin polymer films. Fig. 7b shows the surface

excess compositions of CH_2, CF_2 and CF_3 groups (with respect to the bulk) at the interface (the interface region is considered to be 1.8 nm below the air-polymer interface; see Fig. 7a and Section I of SI for more details) of pNBFn polymers calculated from MD simulations. These specific groups were analyzed because they are known to have the most impact on surface wettability.

As shown in Fig. 7b from calculations described in **Section I**, **Supporting Information**, the surface of the pNBFn polymers is significantly CF_3 enriched. These polymers show preferential segregation of CF_3 over CF_2 groups, which is expected since chain ends are known to segregate on the surface to maximize conformational entropy [64]. The preferential segregation of CF_3 may also be due to enthalpic effects. CF_3 groups have low cohesive energy and could be expelled to the surface to minimize the overall enthalpy. This preferential segregation is insensitive to chain length beyond 4, which could be due to enthalpy-entropy tradeoff. Although, preferential segregation of CF_3 groups may be enthalpically favorable, for longer side chains, this may be associated with entropic penalty (longer side chains prefer to remain in the bulk). In the case of pNB, the surface compositon of CH_2 is close to that of the bulk (i.e., surface excess composition is close to 0) while a depletion of CH_2 is observed in pNBFn polymers (i.e., surface excess compositions are negative).

Examining the orientation of the perfluoro side chains in the interfacial region from the distribution the angle θ between the vector joining the two ends of the carbon atoms of the side chain and the normal to the x-y plane (Fig. 7c), we find the chains on average preferably orient towards the surface (mean values of θ lie between 63° – 67° with a maximum uncertainty of 30°). This is remarkably different from what is seen in the bulk where side chains on average lie parallel to the surface (see discussions in Section 3.1).

The surface wettabilities of the pNBFn films generated using the scROMP process on a gold substrate were measured using contact angle goniometry with water and hexadecane (Fig. 7d). Measurements were also taken on pNBFn films on PAN supports, where the data in Fig. 7d were replicated (Table C1). The preferential segregation of low-energy CF_3 groups combined with depletion of CH_2 groups, as shown from simulations in Fig. 7b, makes fluorinated polymers highly hydrophobic and oleophobic and further reduces the surface energy. As a dispersive probe liquid, hexadecane is extremely sensitive to fluorocarbon groups vs hydrocarbon groups. For example, advancing hexadecane angles on

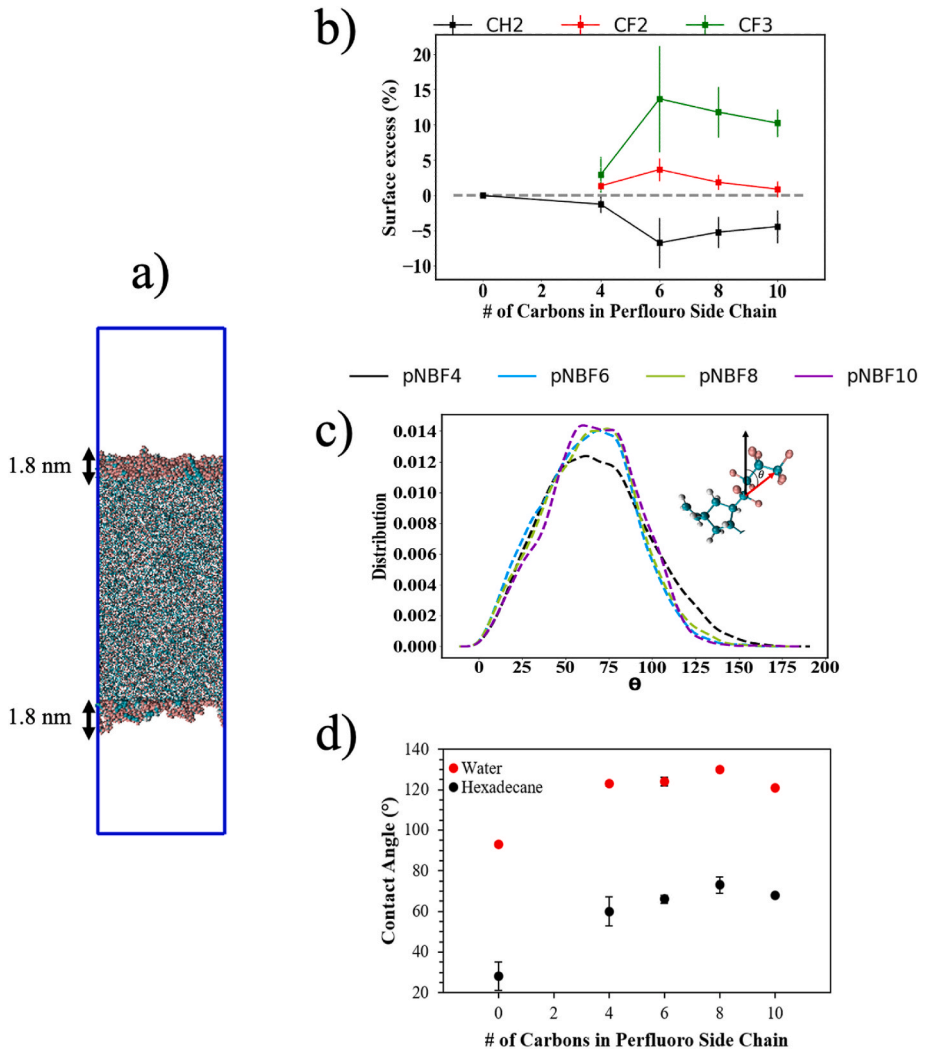

Fig. 7. (a) Simulation snapshot illustrating the interface region defined as the outer 1.8 nm of the polymer at the air polymer interface of the simulation cell (carbon atoms are represented by cyan spheres, hydrogen atoms by white and fluorine by purple; atoms in the interface region are exaggerated) and from which data was collected to calculate the surface excess composition and side-chain surface orientation, (b) excess composition of various chemical groups in the interface region, (c) distribution of the angle θ between the vector joining the two ends of the carbon atoms of the perfluoro chain (denoted by red arrow, see inset) and the normal to the x-y plane (denoted by black arrow), and (d) experimentally measured advancing contact angles of hexadecane and water measured for each polymer on a gold substrate. Error bars not visible fall within the size of the marker. (For interpretation of the references to color in this figure legend, the reader is referred to the Web version of this article.)

surfaces that are predominately –CF_3 (~80°), –CF_2- (~60°), –CH_3 (~50°), and –CH_2- (~20°) exhibit a tremendous range of wettability for surfaces that are all considered to be hydrophobic [65,66]. The addition of the low-energy perfluoro moiety causes a large increase in the advancing contact angle of water from 93° to 123° and of hexadecane from 28° to 60° for pNBF4 as compared to pNB. Further elongation of the fluorocarbon group leads to small increases in contact angle, where maximum values of both water (130°) and hexadecane (73°) are reached at pNBF8 before decreasing slightly from pNBF8 to pNBF10. The trend in hexadecane contact angles in Fig. 7d is consistent with the critical surface tensions (γ_c) of these films as 18, 16, 8, and 11 mN/m for n = 4, 6, 8, and 10, respectively [32,38]. Since poly(tetrafluoroethylene), an all –CF_2- polymer, exhibits a critical surface tension of 18 mN/m [67], the lower values for pNBFn indicate surfaces with both CF_3 and CF_2 compositions, in agreement with simulations in Fig. 7b. The lowest γ_c for pNBF8 is consistent with a CF_3-dominated surface. Thus, the perfluorooctyl side chain seems to be the optimal length to achieve a dominance of –CF_3 groups on the surface. This optimum chain length of 8 is reasonably due to sufficient length to shield the underlying hydrocarbon backbone, even at the ~65° angle of orientation (Fig. 7c), while possessing a more favorable ratio of –CF_3 to –CF_2- groups along the chain than pNBF10 does.

3.6. Swellability

To assess polymer stability in various solvents, the degree of swelling of each polymer film in the pNBFn system was measured in both polar (water and ethanol) and nonpolar (hexane and toluene) solvents (Fig. 8a). In all solvents, the observed percent swelling at room temperature is significantly reduced with the attachment of a fluorocarbon moiety. This trend is observed because the perfluoroalkyl groups are more effective at repelling liquids as compared to their hydrocarbon counterparts due to their lipophobicity and hydrophobicity [68,69], similar to the contact angle trend observed in Fig. 7d. The lowest swelling is achieved with pNBF6 and pNBF8 in each solvent tested. The most dramatic fluorocarbon-induced reductions of swelling at room temperature are with nonpolar solvents, where pNB swells nearly 30 % in both hexane and toluene and the semifluorinated polymers swell 15 % or less in the same solvents. This finding suggests that the pNBFn polymers can be resistant to potential organic impurities in feed streams and could have application in other areas, such as organic solvent nanofiltration due to their stability in pure hexane and toluene [70].

In light of the minimal sorption of water and ethanol into the pNBFn films at room temperature, the swelling experiments were repeated at 60 °C, a typical pervaporation membrane operating temperature, to probe the operation of these films as ethanol dehydration membranes. We propose that the mechanism of the separation will be governed by two processes described by the solution-diffusion model [13]: 1) a sorption-controlled separation in which the elevated operating temperature will enable the selective sorption of one species into the membrane over the other and 2) a diffusion-controlled process where the smaller species possesses a greater diffusion coefficient than the larger species through the polymer matrix. The results of the swelling study (Fig. 8b) indicate that the polymer films uptake a greater mass of liquid once elevated to a higher temperature. An important consideration to note is the difference in swelling observed between water and ethanol for each polymer as this information will likely inform the sorption selectivity trends of each film. Fig. 8b shows that pNBF8 swells more in water while pNB, pNBF4, pNBF6, and pNBF10 swell to comparable levels in both liquids. Of the films, pNBF8 swells the least in both solvents whereas pNBF10, with only slightly longer fluorocarbon side chain, swells the most. Particularly noteworthy is that pNBF8 swells ~3x more in water than in ethanol at 60 °C, suggesting a strong sorption-based component of selectivity for this polymer film. These results show how a small variation in side-chain length by two CF_2 groups can greatly affect film properties.

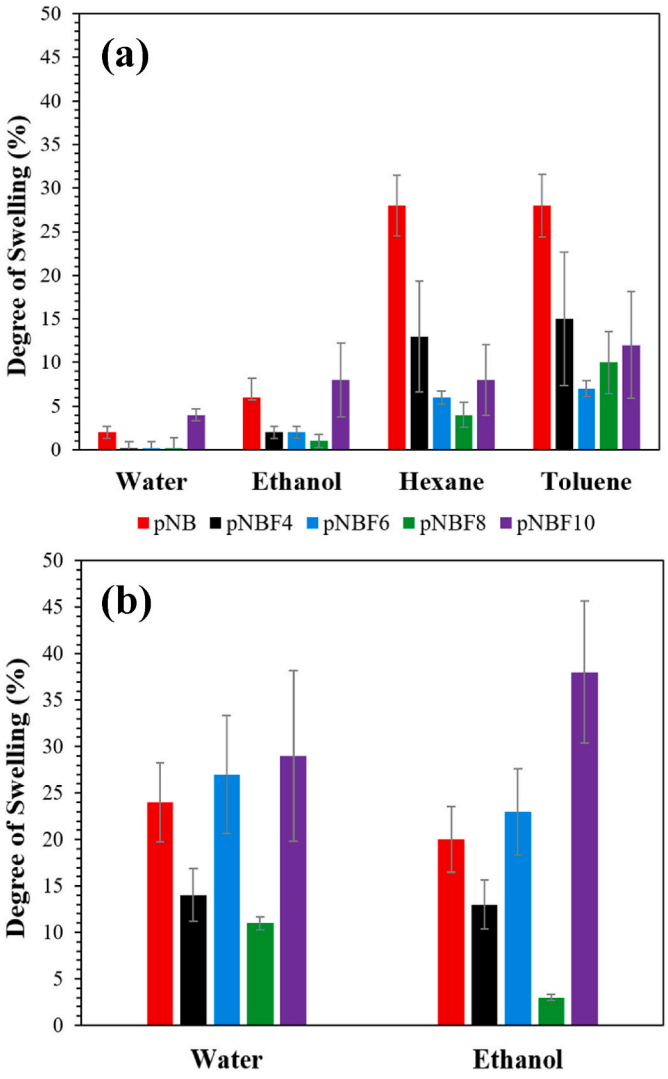

Fig. 8. Percent swelling of polymer films at (a) room temperature and at (b) 60 °C.

3.7. Effect of fluorocarbon chain length on ethanol dehydration via pervaporation

Ethanol dehydration is an important and energy-intensive separation that can greatly benefit from the use of inexpensive membrane technologies. The thermal properties, swelling studies, and stability tests all indicate that pNBFn membranes have the potential for ethanol dehydration while maintaining excellent stability. Each membrane was tested for the dehydration of a 90 wt% ethanol solution at 60 °C, and pNBF6 and pNBF8 were further tested at higher temperatures. Table 4 summarizes the results, showing the total mass flux through the membrane (J), the water permeance ($\frac{P^G_{H_2O}}{l}$), ethanol permeance ($\frac{P^G_{EtOH}}{l}$), membrane selectivity (α) and separation factor (β), and the mass fraction of ethanol in the permeate. For more intuitive comparison, $\frac{P^G_{H_2O}}{l}$, $\frac{P^G_{EtOH}}{l}$, and α for all these membranes at 60 °C are presented as a function of fluorocarbon side chain length in Fig. 9.

pNB is shown to provide almost no separation, as evidenced by the combination of very high water permeance ($\frac{P^G_{H_2O}}{l}$ = 21000 gpu) and very low selectivity (α = 2). This combination of high permeance and low selectivity may be partially due to the instability of pNB during the testing conditions (see **Section E**, **Supporting Information**). The addition of the perfluorobutyl moiety has an effect on the separation

Table 4

Pervaporation performance, including flux (J), water ($\frac{P^G_{H_2O}}{l}$) and ethanol ($\frac{P^G_{EtOH}}{l}$) permeance, selectivity (α), separation factor (β), and weight percentage of ethanol in the permeate, of each polymer for ethanol dehydration. Tests were conducted at various temperatures with a 90 wt% ethanol/water feed.

Polymer	Temperature (°C)	J ($\frac{g}{m^2 h}$)	$\frac{P^G_{H_2O}}{l}$ (GPU)	$\frac{P^G_{EtOH}}{l}$ (GPU)	α	β	Weight Percent EtOH
pNB	60	7100	21000	8700	2	2	85
pNBF4	60	710	1000	258	4	3	75
pNBF6	60	110	400	22	19	13	42
	65	110	280	21	14	10	48
	70	150	300	20	15	11	45
	75	150	240	15	16	12	42
pNBF8	60	110	1000	8	170	60	13
	65	160	1000	6	180	86	10
	70	60	220	4	50	34	21
	75	180	630	4	180	100	8
pNBF10	60	200	800	35	23	15	37

performance, with the flux and water permeance of pNBF4 being an order of magnitude lower and the selectivity marginally improved (α = 4). The weak performance of pNBF4 is attributed to its glassy state that would lead to high non-equilibrium free volume that may hamper diffusional selectivity of water while also increasing the probability for mechanical failure [20]. Significant improvement in separation occurs with the 6-carbon perfluoro side chain length, as the permeate concentration is predominately water and the selectivity rises to α = 19. A further dramatic improvement in separation is observed for pNBF8, where the selectivity at 60 °C rises to α = 170 while obtaining the highest water permeance of the pNBFn membranes ($\frac{P^G_{H_2O}}{l}$ = 1000 GPU). Finally, increasing the fluorocarbon chain length from pNBF8 to pNBF10 enables a higher flux but greatly reduced selectivity (α = 23) and a lower water permeance ($\frac{P^G_{H_2O}}{l}$ = 800 GPU). Thus, the 8-carbon perfluoro side chain achieves the highest selectivity and water permeance of all pNBFn membranes.

As the highest performing membrane, pNBF8 has a unique set of properties that distinguish it from those of pNBF6 and pNBF10. The pNBF8 system achieves the highest contact angles, lowest critical surface tension, lowest swelling, and highest ratio of water to ethanol swelling at 60 °C. The tremendous enhancement in selectivity for pNBF8 compared to the others is attributed in part to the denser packing of the outer fluorocarbon groups in the lower energy pNBF8 film, as determined from its higher hexadecane contact angle (Fig. 7d) and lower critical surface tension (8 mN/m) that indicate a dominance of $-CF_3$ groups on the surface. The ~3x greater mass sorption of water over ethanol at 60 °C (Fig. 8b) is equivalent to an ~8x greater molar sorption of water. Also, given the much smaller size of water vs ethanol, the sorption selectivity for pNBF8 must combine with a strong diffusional selectivity to enable total molar H_2O:EtOH selectivities approaching 200. These results are in general agreement with findings for pNB:pNBF8 copolymers in which we estimated the sorption selectivity of water over ethanol by the perfluorooctyl-dominated outer surface as 18 ± 6 whereas the diffusional selectivity for pNBF8 was 9 ± 6 [38]. The high performance of pNBF8 membranes is also stable upon repeated pervaporation tests of the same membrane over a week (Table F1).

3.8. Temperature effect on pervaporation performance

To explore the effects of temperature on the pervaporation performance, membranes were tested at various operating temperatures. The effect of the feed temperature on the separation performance for pNBF6 and pNBF8 membranes is presented in Table 4. This study indicates that while the selectivity and water permeance were not noticeably improved at higher temperatures, the flux of the pNBFn membranes

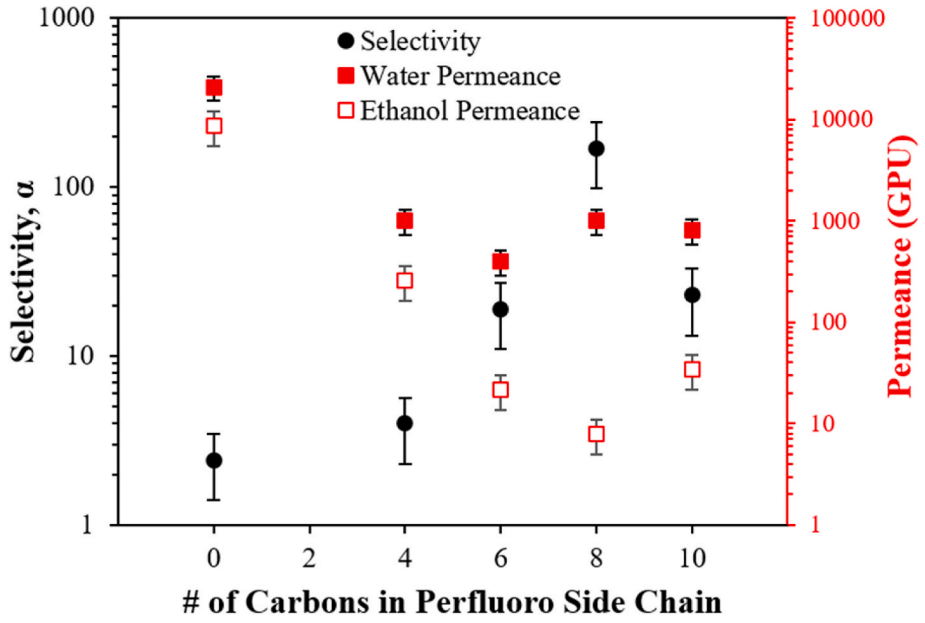

Fig. 9. Effect of fluorocarbon side chain length on membrane selectivity, water permeance, and ethanol permeance from pervaporation tests of a 90 wt% ethanol/water feed at 60 °C.

Table 5

Comparison of pNBF8 to amorphous fluorocarbon membranes from literature for dehydrating 90 wt% ethanol/water mixtures. Flux (J), water ($\frac{P^G_{H_2O}}{l}$) and ethanol ($\frac{P^G_{EtOH}}{l}$) permeance, selectivity (α), and separation factor (β) are provided at the temperature of testing.

Polymer/Support	Temperature (°C)	J ($\frac{g}{m^2h}$)	$\frac{P^G_{H_2O}}{l}$ (GPU)	$\frac{P^G_{EtOH}}{l}$ (GPU)	α	β	Source
pNBF8/PAN	65	160	1000	6	180	86	This work
pNBF8/PAN	75	180	630	4	180	100	This work
CMS-3/PAN	22	920	–	–	–	33	[25]
Cytop	75	–	500	5	110	–	[10]
Hyflon AD	75	–	1100	16	70	–	[10]
Teflon AF	75	–	2900	110	27	–	[10]

generally increased with the temperature of the feed solutions being purified. To gather the temperature effect data, films of pNBF6 and pNBF8 were exposed to operation at various elevated temperatures for more than 40 h of testing. Despite this 40-h exposure to the feed solution and cycling temperatures, when the temperature was reset back to the original operating temperature, no change in performance was detected. This includes the 70 °C data point for pNBF8, where the uncharacteristically low performance was maintained throughout each temperature cycle and for multiple replicates. To further examine the performance at 70 °C, a freshly prepared pNBF8 membrane was tested at 70 °C, yielding a much improved performance, with $\alpha = 250$, $\beta = 110$, and a water permeance of 720 GPU. The results in Table 4, along with those for the repeated testing of pNBF8 over a week (Table F1) and the chemical stability of all pNBFn polymers over shorter times shown in Section F of the Supporting Information, serve as an additional confirmation of the stability of pNBFn membranes. Similar stability has been demonstrated by others for a commercial amorphous perfluoropolymer (APFP) membrane [10]. Here, the notable achievement is the level of performance and solvent stability by a semifluorinated polymer film.

When compared to previous work performed to dehydrate a binary ethanol/water solution using APFPs, the selectivity and separation factor achieved here by pNBF8 is unprecedented (Table 5). For ethanol dehydrations of 90/10 wt% mixtures, the previously highest separation factor was 33 using a CMS-3 film on PAN [25], while the highest selectivity was 110 using Cytop [10]. Here, the performance of top APFPs is achieved and even surpassed by a system that is only semifluorinated, thereby reducing the environmental concerns accompanying perfluorinated substances. The pNBF8 membrane also performs well as compared to hydrophobic membranes in general (see Figure H1). While pNBF8 generally trails the performance of the top hydrophilic membranes, such as PVA, alginate, and chitosan (Figure H1), its robustness and lack of swellability still may be advantageous in certain applications or as a blend with more hydrophilic components.

4. Conclusions

The effect of fluorocarbon side chain length on the properties of semifluorinated polymer membranes was examined with complementary experimental methods, including the measurement of ethanol dehydration by membrane pervaporation, as well as molecular simulations. Polymer films and membranes were successfully and rapidly synthesized using the scROMP process, as confirmed through IR spectroscopy, profilometry, and contact angle goniometry, where the perfluoro side chain greatly increases water and hexadecane contact angles as compared to pNB. SEM images confirm the formation of a dense polymer film that covers the porous PAN support, and profilometry shows that the films conform to the topography of the substrate. All pNBFn films exhibit high thermal stability, and the addition of the fluorocarbon chain greatly increases solvent stability in the typical operating temperature range of ethanol dehydration membranes. For example, pNBF8 films exhibit largely reduced swelling in both polar and non-polar solvents as compared to pNB.

Molecular simulations show that fluorocarbon side chains pack mostly parallel to the film surface in the bulk but more along the surface normal at the outer interface, in agreement with experimental IR spectra and contact angle measurements, respectively. In addition, the simulations show that the presence of the fluorocarbon side chain increases free volume properties at 300 K with only slight dependence on the fluorocarbon chain length.

The ethanol dehydration performance of the pNBFn films is best with a perfluoro chain length of 8, with pNBF8 achieving a selectivity (α) of 180 and water permeance of 1000 gpu at 65 °C. The elevated performance for pNBF8 correlates with its dense, CF_3-rich perfluorocarbon surface that achieves the lowest critical surface tension (8 mN/m) to indicate extreme non-wettability, but also the highest ratio of water to ethanol swelling at 60 °C of the other pNBFn systems studied. Swelling can be expected to be a large contributing factor to membrane selectivity due to the PLD of the neat polymers being smaller than either molecule, thus indicating the need for swelling-induced enlargement of pores to facilitate component transport. The results are consistent with a dense outer layer that strongly regulates transport but favors the much smaller water molecule over ethanol. Remarkably, this selectivity of pNBF8 is greater than those reported in the literature for APFPs to date, in addition to reducing PFAS risk by the semifluorinated status and its ability to mix with norbornene to achieve random copolymers with lower flurorocarbon content but identical surface properties [38]. Furthermore, the integrity of pNBFn films is maintained through operation at various elevated temperatures for more than 40 h of testing.

The performance of the pNBF8 membranes offers significant benefits that will be explored in future work, both as a stand-alone homopolymer and as a component in polymer blends or co-polymerizations. Furture efforts will also be devoted towards understanding the effect of local structure on the sorption-diffusion phenomena occurring in pNBFn polymers using molecular models developed in this work. The pNBFn polymers could serve as organic solvent nanofiltration membranes and as protective barriers for polymers prone to high degrees of swelling.

CRediT authorship contribution statement

Tyler D. Oddo: Writing – review & editing, Writing – original draft, Visualization, Validation, Methodology, Investigation, Formal analysis, Data curation. **Arun Srikanth:** Writing – review & editing, Writing – original draft, Visualization, Software, Methodology, Investigation, Formal analysis. **Zane J. Parkerson:** Writing – review & editing, Resources, Methodology, Investigation. **Matthew P. Vasuta:** Writing – review & editing, Validation, Methodology, Investigation. **Co D. Quach:** Writing – review & editing, Investigation. **Clare McCabe:** Writing – review & editing, Software, Project administration, Methodology, Funding acquisition, Conceptualization. **G. Kane Jennings:** Writing – review & editing, Supervision, Resources, Project administration, Methodology, Funding acquisition, Conceptualization.

Declaration of competing interest

The authors declare that they have no known competing financial interests or personal relationships that could have appeared to influence the work reported in this paper.

Acknowledgments

The authors would like to thank the National Science Foundation (NSF) for funding this project through the Division of Materials Research (Award #2119575) for all authors and the Graduate Research Fellowship Program for Z.J.P. We thank the Vanderbilt Undergraduate Summer Research Program for a fellowship for T.D.O. The funding sources had no involvement in the design, data collection, writing, or submission of the work in this study. The authors also thank the Vanderbilt Institute of Nanoscale Science and Engineering (VINSE) for the use of their characterization tools and technical support. The authors acknowledge the use of the HWU high performance computing facility (DMOG) and associated support services in the completion of this work. Additional gratitude is given to Dr. Paul Voziyan and Dr. Aaron Daniel for their assistance with the collection of thermal property data.

Appendix A. Supplementary Data

Supplementary data to this article can be found online at https://doi.org/10.1016/j.memsci.2025.124367. Included in this document is an analysis of the optimal catalyst spin speed, a description of how the Bondi fractional free volume of the polymer films was calculated, contact angle measurements on pNBF4 and pNBF6 films on gold versus on PAN substrates, a pervaporation experimental setup schematic, lower magnification SEM image, EDS electron image, membrane stability testing, differential scanning calorimetry scans of pNB and pNBFn, comparison of pNBFn performance in ethanol dehydration with other top membranes, and detailed information regarding simulation methods.

Data availability

Data will be made available on request.

References

[1] J. Baeyens, Q. Kang, L. Appels, R. Dewil, Y. Lv, T. Tan, Challenges and opportunities in improving the production of bio-ethanol, Prog. Energy Combust. Sci. 47 (2015) 60–88, https://doi.org/10.1016/j.pecs.2014.10.003.
[2] S. Lee (Ed.), Encyclopedia of Chemical Processing (Online), CRC Press, Boca Raton, 2005, https://doi.org/10.1201/NOE0824755638.
[3] A. Singh, G.P. Rangaiah, Development and optimization of a novel process of double-effect distillation with vapor recompression for bioethanol recovery and vapor permeation for bioethanol dehydration, J. Chem. Technol. Biotechnol. 94 (2019) 1041–1056, https://doi.org/10.1002/jctb.5851.
[4] M.J. Bradshaw, Global energy dilemmas: a geographical perspective, Geogr. J. 176 (2010) 275–290, https://doi.org/10.1111/j.1475-4959.2010.00375.x.
[5] Ó.J. Sánchez, C.A. Cardona, Trends in biotechnological production of fuel ethanol from different feedstocks, Bioresour. Technol. 99 (2008) 5270–5295, https://doi.org/10.1016/j.biortech.2007.11.013.
[6] M.O.S. Dias, T.L. Junqueira, C.E.V. Rossell, R. Maciel Filho, A. Bonomi, Evaluation of process configurations for second generation integrated with first generation bioethanol production from sugarcane, Fuel Process. Technol. 109 (2013) 84–89, https://doi.org/10.1016/j.fuproc.2012.09.041.
[7] H.-J. Huang, S. Ramaswamy, U.W. Tschirner, B.V. Ramarao, A review of separation technologies in current and future biorefineries, Sep. Purif. Technol. 62 (2008) 1–21, https://doi.org/10.1016/j.seppur.2007.12.011.
[8] Q. Kang, B. Van der Bruggen, R. Dewil, J. Baeyens, T. Tan, Hybrid operation of the bio-ethanol fermentation, Sep. Purif. Technol. 149 (2015) 322–330, https://doi.org/10.1016/j.seppur.2015.05.007.
[9] T. Roth, P. Kreis, A. Górak, Process analysis and optimisation of hybrid processes for the dehydration of ethanol, Chem. Eng. Res. Des. 91 (2013) 1171–1185, https://doi.org/10.1016/j.cherd.2013.01.016.
[10] Y. Huang, J. Ly, D. Nguyen, R.W. Baker, Ethanol dehydration using hydrophobic and hydrophilic polymer membranes, Ind. Eng. Chem. Res. 49 (2010) 12067–12073, https://doi.org/10.1021/ie100608s.
[11] W.-C. Chao, Y.-H. Huang, D.-J. Liaw, Y.-Y. Hsieh, W.-S. Hung, S.-H. Huang, et al., Correlating the microstructure of novel polyamide thin-film composite membranes with ethanol dehydration performances, Polymer 54 (2013) 1381–1387, https://doi.org/10.1016/j.polymer.2013.01.011.
[12] L. Liu, S.E. Kentish, Pervaporation performance of crosslinked PVA membranes in the vicinity of the glass transition temperature, J. Membr. Sci. 553 (2018) 63–69, https://doi.org/10.1016/j.memsci.2018.02.021.
[13] J.G. Wijmans, R.W. Baker, The solution-diffusion model: a review, J. Membr. Sci. 107 (1995) 1–21, https://doi.org/10.1016/0376-7388(95)00102-I.
[14] Q. Kang, J. Huybrechts, B. Van der Bruggen, J. Baeyens, T. Tan, R. Dewil, Hydrophilic membranes to replace molecular sieves in dewatering the bio-ethanol/water azeotropic mixture, Sep. Purif. Technol. 136 (2014) 144–149, https://doi.org/10.1016/j.seppur.2014.09.009.
[15] D.S. Sholl, R.P. Lively, Seven chemical separations to change the world, Nature 532 (2016) 435–437, https://doi.org/10.1038/532435a.
[16] L. Wang, M.S.H. Boutilier, P.R. Kidambi, D. Jang, N.G. Hadjiconstantinou, R. Karnik, Fundamental transport mechanisms, fabrication and potential applications of nanoporous atomically thin membranes, Nat. Nanotechnol. 12 (2017) 509–522, https://doi.org/10.1038/nnano.2017.72.
[17] L. Prozorovska, P.R. Kidambi, State-of-the-Art and future prospects for atomically thin membranes from 2D materials, Adv. Mater. 30 (2018) 1801179, https://doi.org/10.1002/adma.201801179.
[18] Billmeyer, Textbook of Polymer Science, Wiley India Pvt. Limited, 2007.
[19] E.H. Cordes, H.G. Bull, Mechanism and catalysis for hydrolysis of acetals, ketals, and ortho esters, Chem. Rev. 74 (1974) 581–603, https://doi.org/10.1021/cr60291a004.
[20] M. Imad, R. Castro-Muñoz, Ongoing progress on pervaporation membranes for ethanol separation, Membranes 13 (2023) 848, https://doi.org/10.3390/membranes13100848.
[21] H. Heydari, S. Salehian, S. Amiri, M. Soltanieh, S.A. Musavi, UV-cured polyvinyl alcohol-MXene mixed matrix membranes for enhancing pervaporation performance in dehydration of ethanol, Polym. Test. 123 (2023) 108046, https://doi.org/10.1016/j.polymertesting.2023.108046.
[22] L.M. Vane, Review: membrane materials for the removal of water from industrial solvents by pervaporation and vapor permeation, J. Chem. Technol. Biotechnol. Oxf. Oxfs. 94 (1986 2019) 343–365, https://doi.org/10.1002/jctb.5839.
[23] J. Tang, K.K. Sirkar, S. Majumdar, Pervaporative dehydration of concentrated aqueous solutions of selected polar organics by a perfluoropolymer membrane, Sep. Purif. Technol. 175 (2017) 122–129, https://doi.org/10.1016/j.seppur.2016.10.032.
[24] T.A. Jalal, N.M.S. Bettahalli, N.L. Le, S.P. Nunes, Hydrophobic hyflon AD/Poly (vinylidene fluoride) membranes for butanol dehydration via pervaporation, Ind. Eng. Chem. Res. 54 (2015) 11180–11187, https://doi.org/10.1021/acs.iecr.5b02754.
[25] V. Smuleac, J. Wu, S. Nemser, S. Majumdar, D. Bhattacharyya, Novel perfluorinated polymer-based pervaporation membranes for the separation of solvent/water mixtures, J. Membr. Sci. 352 (2010) 41–49, https://doi.org/10.1016/j.memsci.2010.01.058.
[26] Y. Huang, R.W. Baker, J.G. Wijmans, Perfluoro–coated hydrophilic membranes with improved selectivity, Ind. Eng. Chem. Res. 52 (2013) 1141–1149, https://doi.org/10.1021/ie3020654.
[27] A.M. Calafat, L.-Y. Wong, Z. Kuklenyik, J.A. Reidy, L.L. Needham, Polyfluoroalkyl chemicals in the U.S. population: data from the national health and nutrition examination survey (NHANES) 2003–2004 and comparisons with NHANES 1999–2000, Environ. Health Perspect. 115 (2007) 1596–1602, https://doi.org/10.1289/ehp.10598.
[28] E.M. Sunderland, X.C. Hu, C. Dassuncao, A.K. Tokranov, C.C. Wagner, J.G. Allen, A review of the pathways of human exposure to poly- and perfluoroalkyl substances (PFASs) and present understanding of health effects, J. Expo. Sci. Environ. Epidemiol. 29 (2019) 131–147, https://doi.org/10.1038/s41370-018-0094-1.
[29] E. Perez, Synthesis of bicyclo [2*2*1] Hept-2-enes with Mono and disubstituted long perfluorinated chains CnF2n+1 (n = 4,6,8,10) investigation of association in solution by 19F NMR study of polymerization via A metathetic reaction, J. Fluor. Chem. 39 (1988) 173–196.
[30] B.J. Berron, C.J. Faulkner, R.E. Fischer, P.A. Payne, G.K. Jennings, Surface-initiated growth of ionomer films from Pt-Modified gold electrodes, Langmuir 25 (2009) 12721–12728, https://doi.org/10.1021/la901809f.
[31] C.J. Faulkner, P.A. Payne, G.K. Jennings, Surface-initiated ring-opening metathesis polymerization of 5-(perfluorohexyl)norbornene on carbon paper electrodes, J. Colloid Interface Sci. 351 (2010) 248–253, https://doi.org/10.1016/j.jcis.2010.07.044.
[32] C.J. Faulkner, R.E. Fischer, G.K. Jennings, Surface-initiated polymerization of 5-(Perfluoro-n-alkyl)norbornenes from gold substrates, Macromolecules 43 (2010) 1203–1209, https://doi.org/10.1021/ma902249m.
[33] C.A. Escobar, M.P. Spellings, T.J. Cooksey, G.K. Jennings, Reproducing superhydrophobic leaves as coatings by micromolding surface-initiated polymerization, Macromol. Rapid Commun. 35 (2014) 1937–1942, https://doi.org/10.1002/marc.201400412.
[34] Y. Cho, Y. Kim, T.-L. Choi, J. Lim, K. Char, Swelling-induced pore generation in fluorinated polynorbornene block copolymer films, Polym. Chem. 9 (2018) 3536–3542, https://doi.org/10.1039/C8PY00646F.
[35] X. Lin, J. Shi, Z. Shi, S. Niwayama, Hydrophobic and antifouling modification of graphene oxide with functionalized polynorbornene by surface-initiated ring-opening metathesis polymerization, New J. Chem. 46 (2022) 5806–5818, https://doi.org/10.1039/D1NJ05935A.

[36] D. Cao, X. Sun, H. Gao, L. Pan, N. Li, Y. Li, Crosslinked polynorbornene-based anion exchange membranes with perfluorinated branch chains, Polymers 15 (2023) 1073, https://doi.org/10.3390/polym15051073.
[37] O.A. Adzhieva, Nikiforov Ryu, M.L. Gringolts, N.A. Belov, M.P. Filatova, Denisova YuI, et al., Synthesis and gas separation properties of metathesis Poly(5-perfluorobutyl-2-norbornene), Polym. Sci. 64 (2022) 424–433, https://doi.org/10.1134/S0965545X22700262.
[38] M.P. Vasuta, Z.J. Parkerson, T.D. Oddo, B.R. Rogers, G.K. Jennings, Fluorocarbon minimization via semifluorinated copolymer films by combining spin coating and ring-opening metathesis polymerization, Langmuir 41 (2025) 6931–6943, https://doi.org/10.1021/acs.langmuir.4c05253.
[39] Z.J. Parkerson, L. Prozorovska, M.P. Vasuta, T.D. Oddo, G.K. Jennings, Simultaneous spin coating and ring-opening metathesis polymerization for the rapid synthesis of polymer films, ACS Appl. Mater. Interfaces (2024), https://doi.org/10.1021/acsami.4c00211.
[40] K. Satake, K. Usumoto, K. Hikasa, M. Kimura, N. Kishima, S. Morosawa, The diels-alder reaction of Cycloocta- and Cyclonona-1,3-diene with maleic anhydride using hydroquinone as a polymerization inhibiting catalyst, ChemInform 23 (1992), https://doi.org/10.1002/chin.199245089.
[41] J.A. Love, J.P. Morgan, T.M. Trnka, R.H. Grubbs, A practical and highly active ruthenium-based catalyst that effects the cross metathesis of acrylonitrile, Angew Chem. Int. Ed. Engl. 41 (2002) 4035–4037, https://doi.org/10.1002/1521-3773(20021104)41:21<4035::AID-ANIE4035>3.0.CO;2-I.
[42] X. Deng, L. Prozorovska, G.K. Jennings, Metal chelating polymer thin films by surface-initiated ROMP and modification, J. Phys. Chem. C 123 (2019) 23511–23519, https://doi.org/10.1021/acs.jpcc.9b06410.
[43] Spin coating: complete guide to theory and techniques. Ossila n.d. https://www.ossila.com/pages/spin-coating (accessed March 13, 2024).
[44] R.W. Baker, J.G. Wijmans, Y. Huang, Permeability, permeance and selectivity: a preferred way of reporting pervaporation performance data, J. Membr. Sci. 348 (2010) 346–352, https://doi.org/10.1016/j.memsci.2009.11.022.
[45] P.T. Cummings, C. McCabe, C.R. Iacovella, A. Ledeczi, E. Jankowski, A. Jayaraman, et al., Open-source molecular modeling software in chemical engineering focusing on the molecular simulation design framework, AIChE J. 67 (2021) e17206, https://doi.org/10.1002/aic.17206.
[46] M.W. Thompson, J.B. Gilmer, R.A. Matsumoto, C.D. Quach, P. Shamaprasad, A. H. Yang, et al., Towards molecular simulations that are transparent, reproducible, useable by others, and extensible (TRUE), Mol. Phys. 118 (2020) e1742938, https://doi.org/10.1080/00268976.2020.1742938.
[47] A.Z. Summers, J.B. Gilmer, C.R. Iacovella, P.T. Cummings, C. McCabe, MoSDeF, a python framework enabling large-scale computational screening of soft matter: application to chemistry-property relationships in lubricating monolayer films, J. Chem. Theor. Comput. 16 (2020) 1779–1793, https://doi.org/10.1021/acs.jctc.9b01183.
[48] W.L. Jorgensen, D.S. Maxwell, J. Tirado-Rives, Development and testing of the OPLS all-atom force field on conformational energetics and properties of organic liquids, J. Am. Chem. Soc. 118 (1996) 11225–11236, https://doi.org/10.1021/ja9621760.
[49] C. Klein, A.Z. Summers, M.W. Thompson, J.B. Gilmer, C. McCabe, P.T. Cummings, et al., Formalizing atom-typing and the dissemination of force fields with foyer, Comput. Mater. Sci. 167 (2019) 215–227, https://doi.org/10.1016/j.commatsci.2019.05.026.
[50] S. Páll, A. Zhmurov, P. Bauer, M. Abraham, M. Lundborg, A. Gray, et al., Heterogeneous parallelization and acceleration of molecular dynamics simulations in GROMACS, J. Chem. Phys. 153 (2020) 134110, https://doi.org/10.1063/5.0018516.
[51] L.J. Abbott, K.E. Hart, C.M. Colina, Polymatic: a generalized simulated polymerization algorithm for amorphous polymers, Theor. Chem. Acc. 132 (2013) 1334, https://doi.org/10.1007/s00214-013-1334-z.
[52] Z. Li, F. Yuan, K.A. Fichthorn, S.T. Milner, R.G. Larson, Molecular view of Polymer/water interfaces in latex paint, Macromolecules 47 (2014) 6441–6452, https://doi.org/10.1021/ma500866f.
[53] R.M. Silverstein, F.X. Webster, D. Kiemle, Spectrometric Identification of Organic Compounds, seventh ed., Wiley, 2005.
[54] N.A. Belov, M.L. Gringolts, A.A. Morontsev, L.E. Starannikova, Yampolskii YuP, Finkelstein Esh, Gas-transport properties of epoxidated metathesis polynorbornenes, Polym. Sci. B 59 (2017) 560–569, https://doi.org/10.1134/S1560090417050025.
[55] X. Wang, J. Wilson T, D. Alentiev, M. Gringolts, E. Finkelshtein, M. Bermeshev, et al., Substituted polynorbornene membranes: a modular template for targeted gas separations, Polym. Chem. 12 (2021) 2947–2977, https://doi.org/10.1039/D1PY00278C.
[56] J.E. Mark, Polymer Data Handbook, second ed., Oxford University Press, Oxford, New York, 2009.
[57] M.A. Esteruelas, F. González, J. Herrero, P. Lucio, M. Oliván, B. Ruiz-Labrador, Thermal properties of polynorbornene (cis- and trans-) and hydrogenated polynorbornene, Polym. Bull. 58 (2007) 923–931, https://doi.org/10.1007/s00289-007-0734-4.
[58] J.D. Hatjopoulos, R.A. Register, Synthesis and properties of well-defined elastomeric Poly(alkylnorbornene)s and their hydrogenated derivatives, Macromolecules 38 (2005) 10320–10322, https://doi.org/10.1021/ma0515331.
[59] P.J. Flory, M. Volkenstein, Statistical mechanics of chain molecules, Biopolymers 8 (1969) 699–700, https://doi.org/10.1002/bip.1969.360080514.
[60] J. Paturej, S.S. Sheiko, S. Panyukov, M. Rubinstein, Molecular structure of bottlebrush polymers in melts, Sci. Adv. 2 (2016) e1601478, https://doi.org/10.1126/sciadv.1601478.
[61] M.L. Greenfield, D.N. Theodorou, Geometric analysis of diffusion pathways in glassy and melt atactic polypropylene, Macromolecules 26 (1993) 5461–5472, https://doi.org/10.1021/ma00072a026.
[62] D. Hofmann, M. Entrialgo-Castano, A. Lerbret, M. Heuchel, Y. Yampolskii, Molecular modeling investigation of free volume distributions in stiff chain polymers with conventional and ultrahigh free volume: Comparison between molecular modeling and positron lifetime studies, Macromolecules 36 (2003) 8528–8538, https://doi.org/10.1021/ma034971l.
[63] L. Sarkisov, R. Bueno-Perez, M. Sutharson, D. Fairen-Jimenez, Materials informatics with PoreBlazer v4.0 and the CSD MOF database, Chem. Mater. 32 (2020) 9849–9867, https://doi.org/10.1021/acs.chemmater.0c03575.
[64] S. Lee, C.W. Frank, D.Y. Yoon, Interface characteristics of neat melts and binary mixtures of polyethylenes from atomistic molecular dynamics simulations, Polymers 12 (2020) 1059, https://doi.org/10.3390/polym12051059.
[65] E.L. Brantley, G.K. Jennings, Fluorinated polymer films from acylation of ATRP surface-initiated Poly(hydroxyethyl methacrylate), Macromolecules 37 (2004) 1476–1483, https://doi.org/10.1021/ma035471v.
[66] E.L. Brantley, T.C. Holmes, G.K. Jennings, Modification of ATRP surface-initiated Poly(hydroxyethyl methacrylate) films with hydrocarbon side chains, J. Phys. Chem. B 108 (2004) 16077–16084, https://doi.org/10.1021/jp0476038.
[67] A.K. Roy Choudhury (Ed.), Principles of Textile Finishing, Woodhead Publishing, 2017, https://doi.org/10.1016/B978-0-08-100646-7.09991-4.
[68] J.N. Israelachvili, Intermolecular and Surface Forces, Academic Press, 2010.
[69] M.P. Krafft, J.G. Riess, Perfluorocarbons: life sciences and biomedical uses, J. Polym. Sci. Part Polym Chem 45 (2007) 1185–1198, https://doi.org/10.1002/pola.21937.
[70] G.M. Shi, Y. Feng, B. Li, H.M. Tham, J.-Y. Lai, T.-S. Chung, Recent progress of organic solvent nanofiltration membranes, Prog. Polym. Sci. 123 (2021) 101470, https://doi.org/10.1016/j.progpolymsci.2021.101470.